De Novo Serine Synthesis Is a Metabolic Vulnerability That Can Be Exploited to Overcome Sunitinib Resistance in Advanced Renal Cell Carcinoma

Manon Teisseire[1], Umakant Sahu[2,3], Julien Parola[1], Meng-Chen Tsai[1], Valérie Vial[4], Jérôme Durivault[4], Renaud Grépin[4], Yann Cormerais[5], Clément Molina[1], Arthur Gouraud[1], Gilles Pagès[1], Issam Ben-Sahra[2,3], and Sandy Giuliano[1]

ABSTRACT

Sunitinib is an oral tyrosine kinase inhibitor used in treating advanced renal cell carcinoma (RCC) that exhibits significant efficacy but faces resistance in 30% of patients. Identifying the molecular mechanisms underlying resistance could enable the development of strategies to enhance sunitinib sensitivity. In this study, we showed that sunitinib induces a metabolic shift leading to increased serine synthesis in RCC cells. Activation of the GCN2–ATF4 stress response pathway was identified as the mechanistic link between sunitinib treatment and elevated serine production. The increased serine biosynthesis supported nucleotide synthesis and sustained cell proliferation, migration, and invasion following sunitinib treatment. Inhibiting key enzymes in the serine synthesis pathway, such as phosphoglycerate dehydrogenase and phosphoserine aminotransferase 1, enhanced the sensitivity of resistant cells to sunitinib. Beyond RCC, similar activation of serine synthesis following sunitinib treatment occurred in a variety of other cancer types, suggesting a shared adaptive response to sunitinib therapy. Together, this study identifies the *de novo* serine synthesis pathway as a potential target to overcome sunitinib resistance, offering insights into therapeutic strategies applicable across diverse cancer contexts.

Significance: Sunitinib treatment induces metabolic reprogramming to provide essential metabolite building blocks for tumor survival, resistance, and progression by upregulating serine biosynthesis, which represents a targetable dependency to enhance therapeutic efficacy.

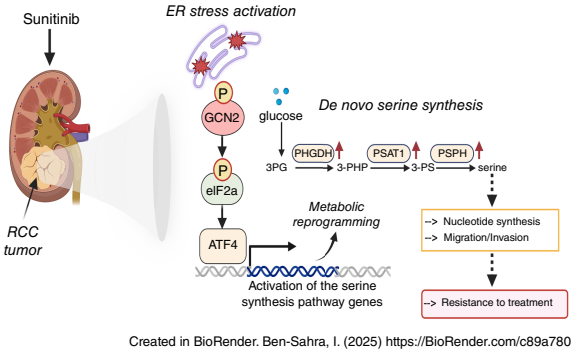

Created in BioRender. Ben-Sahra, I. (2025) https://BioRender.com/c89a780

Introduction

Clear cell renal cell carcinoma (ccRCC), which accounts for 80% of kidney cancer cases, is primarily driven by mutations in the Von Hippel–Lindau (*VHL*) and polybromo-1 gene (1–3). Inactivation of VHL leads to the stabilization of hypoxia-inducible factors 1α and 2α (HIF1α/HIF2α), which promote angiogenesis, migration, invasion, and metabolic reprogramming. Factors such as smoking, dialysis dependence, prolonged painkiller use, hypertension, obesity, and diabetes often contribute to the development of these mutations. Loss of VHL or polybromo-1 enhances glycolysis, progrowth signaling, and cholesterol biosynthesis in tumor cells (4–6). Cancer cells, characterized by high glucose uptake, rely on this metabolic reprogramming to produce ATP and key metabolic intermediates such as dihydroxyacetone phosphate, serine, glycine, and ribose 5-phoshate, which are essential substrates for lipids and nucleotide synthesis, facilitating cell proliferation (7, 8).

In the late 2000s, metastatic ccRCC exhibited a poor prognosis, with a median survival of approximately only 13 months and a 5-year survival rate below 10%. This dismal outcome primarily stemmed from the limited efficacy of traditional chemotherapy and radiotherapy. However, the introduction of antiangiogenic drugs and immunotherapies has improved survival rates, though metastatic ccRCC remains incurable (9). Tyrosine kinase inhibitors (TKI) such as sunitinib and pazopanib are the standard of care for metastatic ccRCC due to their effectiveness in targeting the VEGFR and other tyrosine kinase receptors. However, despite their initial success, resistance to these therapies inevitably arises through mechanisms that restore angiogenesis and altered drug bioavailability (10–13). Despite

[1]Université Nice Côte d'Azur, Institute for Research on Cancer and Aging of Nice (IRCAN) UMR CNRS 7284/U1081, INSERM, Centre Antoine Lacassagne, Nice, France. [2]Department of Biochemistry and Molecular Genetics, Feinberg School of Medicine, Northwestern University, Chicago, Illinois. [3]Robert H. Lurie Comprehensive Cancer Center, Northwestern University, Chicago, Illinois. [4]Centre Scientifique de Monaco, Biomedical Department, Monaco. [5]Department of Molecular Metabolism, Harvard T.H. Chan School of Public Health, Boston, Massachusetts.

Corresponding Authors: Sandy Giuliano, Centre Antoine Lacassagne - Bât B, Institute of Research on Cancer and Aging in Nice, 33 Avenue de Valombrose, Nice 06189, Alpes-Maritimes, France. E-mail: sandy.giuliano@univ-cotedazur.fr; and Issam Ben-Sahra, Simpson Querrey Institute, Room 7-520, 303 E Superior, Chicago, IL 60611. E-mail: issam.ben-sahra@northwestern.edu

Cancer Res 2025;85:1857–73

doi: 10.1158/0008-5472.CAN-24-1393

these insights, the precise molecular causes of sunitinib resistance in ccRCC remain incompletely understood.

Interestingly, ccRCC exhibits dynamic metabolism, with HIF1α driving increased aerobic glycolysis, lipid accumulation, and glycogen storage (14). Yet, the alteration of other metabolic pathways in ccRCC and whether a specific pathway contributes to sunitinib resistance remain to be demonstrated. Therefore, we hypothesize that ccRCC cells adapt to sunitinib treatment by activating compensatory anabolic pathways, which enable continued proliferation and resistance.

One such pathway is the serine–glycine one-carbon cycle, which originates from glycolysis and provides crucial substrates for nucleotide synthesis, redox homeostasis, and methylation reactions that modulate the epigenetic landscape (15–18). This pathway is vital for cancer proliferation, and enzymes involved in serine biosynthesis, such as phosphoglycerate dehydrogenase (PHGDH), are frequently amplified or overexpressed in various cancers (18–27).

Through the integration of RNA sequencing (RNA-seq) and metabolite profiling data, we identified a distinct metabolic adaptive response to sunitinib treatment in ccRCC cells. Our results show a significant increase in serine levels, driven by enhanced endogenous synthesis, in both sunitinib-sensitive and -resistant ccRCC cells. This metabolic rewiring enables the cells to partially evade the inhibitory effects of sunitinib and supports tumor progression. Beyond ccRCC, we observed similar increases in serine synthesis across other cancer models, including triple-negative breast cancer (TNBC), lung cancer, medulloblastoma, and head and neck cancer. Mechanistically, the effects of sunitinib are mediated by the activation of the GCN2–ATF4 signaling axis within the integrated stress response (ISR) pathway. This activation subsequently upregulates serine synthesis enzymes, propelling an increase in serine production. The induction of serine synthesis serves as a compensatory mechanism, enabling cells to overcome autophagy defects and support nucleotide synthesis for sustained proliferation and tumor progression. Importantly, direct blockade of serine biosynthesis not only impedes tumor growth but also restricts cell migration and invasion. Our findings suggest that targeting the serine synthesis pathway could be a promising therapeutic approach for overcoming sunitinib resistance in advanced ccRCC. This metabolic reprogramming represents a key vulnerability that can be exploited for more effective cancer treatments.

Materials and Methods

Sunitinib came from residual materials given to patients (Centre Antoine Lacassagne, Nice, France) and prepared as a 2.5 mmol/L stock solution in DMSO (Sigma-Aldrich) and stored at −20°C. Chloroquine (C6628) was purchased from Sigma-Aldrich and NCT-503 from MedChemTronica (HY-101966).

Anti-PHGDH (14719-1-AP, RRID: AB_2283938), anti-phosphoserine phosphatase (PSPH; 14513-1-AP, RRID: AB_2171464), anti-SHMT1 (14149-1-AP, RRID: AB_2239222), anti-SHMT2 (11099-1-AP, RRID: AB_2188452), anti-actin (66009-1-Ig, RRID:AB_2687938), and anti–α-tubulin (66031-1-Ig, RRID: AB_11042766) were obtained from Proteintech. Anti-GCN2 (#3302, RRID: AB_2277617), anti-peIF2 (#3398, RRID: AB_2096481), anti-ATF4 (#11815, RRID: AB_2616025), anti-S6K (#9202, RRID: AB_331676), anti-HSP60 (#12165, RRID: AB_2636980), and anti-HSP90 (#4877, RRID: AB_2233307) were purchased from Cell Signaling Technology. Anti-pGCN2 (#75836, RRID: AB_1310260) and anti-eIF2 (#5369, RRID: AB_304838) were obtained from Abcam. Anti-PSAT1 was obtained from Invitrogen (PA5-22124, RRID: AB_11153526).

Cell culture

Human RCC 786-O cell line (CRL-1932, RRID: CVCL_1051) and A498 cell line (HTB-44, RRID: CVCL_1056) were purchased from the ATCC, and RCC10 cells were a kind gift from W.H. Kaelin (Dana-Farber Cancer Institute, RRID: CVCL_6265). RCC cells were grown in high-glucose DMEM, GlutaMAX Supplement, and pyruvate and supplemented with 7% FBS. Resistant cells were obtained by a chronic exposition to increasing concentrations of sunitinib up to 8 μmoL/L. Primary human RCC cells (isolated by enzymatic dissociation from the exeresis of the operative specimen obtained owing to Dr. D. Ambrosetti, Department of Pathology, University Hospital of Nice, Nice, France) were grown in PromoCell Renal Epithelial Cell Growth Medium 2 (PromoCell).

CAL33 human head and neck squamous cell carcinoma cells, a human head and neck cancer cell line, was purchased from DSMZ (HTB-186, RRID:CVCL_1108). Cells were cultured in high-glucose DMEM, GlutaMAX Supplement, and pyruvate and supplemented with 7% FBS.

Human medulloblastoma cell line Daoy (HTB-186, RRID: CVCL_1167) was purchased from the ATCC and maintained in minimum essential medium with GlutaMAX (Thermo Fisher Scientific, Montigny-le-Bretonneux) supplemented with 10% FBS and 1 mmol/L sodium pyruvate.

The TNBC cell line BT-549 (HTB-122, RRID: CVCL1092) was obtained from the ATCC and was cultured in high-glucose DMEM, GlutaMAX Supplement, and pyruvate and supplemented with 10% FBS and 1% nonessential amino acid.

A549 cells are lung carcinoma epithelial cells obtained from the ATCC (CRM-CCL-185, RRID: CVCL_0023) and grown in high-glucose DMEM, GlutaMAXTM Supplement, and pyruvate and supplemented with 7% FBS.

All cells were grown at 37°C in a humidified atmosphere containing 5% CO_2. All cell lines used in the study were tested and confirmed to be negative for *Mycoplasma* contamination.

Cell count and viability

Cells were seeded in 12-well plates at a density of 30,000 cells (48 hours) or 15,000 cells (96 hours) per well in media containing 7% FBS and treated with vehicle (DMSO) or sunitinib and/or NCT-503. Cell count and cell viability were assessed using the ADAM-MC apparatus (NanoEntek) based on fluorescent propidium iodide staining according to the manufacturer's instructions. All cell count and viability assays were performed in biological triplicates seeded in technical triplicates for each condition.

CellTiter-Glo

Cells were seeded in 96-well plates at density of 1,000 cells per well in media containing 7% FBS treated with vehicle (DMSO) or sunitinib (2.5 μmol/L) and/or NCT-503 (30 μmol/L). Cell proliferation was measured using CellTiter-Glo at 96 hours. The data were normalized to day 0. All cell proliferation assays were performed in biological triplicates seeded in technical triplicates for each condition.

Immunoblotting

To extract proteins, cells were lysed in ice-cold Triton lysis buffer (40 mmol/L HEPES, pH 7.4, 120 mmol/L NaCl, 1 mmol/L EDTA, 1% Triton X-100, 10 mmol/L glycerol 2-phosphate, 10 mmol/L

sodium pyrophosphate, 0.5 mmol/L sodium orthovanadate, and 50 mmol/L NaF; 1 μmol/L Microcystin-LR and protease inhibitor cocktail were added prior to the lysis of cells) and incubated on ice for 30 minutes. Lysates were centrifuged at 20,000 × *g* for 15 minutes at 4°C. Protein concentrations were quantified by bicinchoninic acid (BCA) assay, and protein lysates were normalized for each experiment. Identical amounts of protein lysates (~15–20 μg) were prepared with the loading buffer (Laemmli buffer), incubated at 95°C on heat block for 5 minutes, and separated on SDS-PAGE and transferred onto nitrocellulose blotting membranes. Membranes were blocked in 5% milk in TBST (50 mmol/L Tris, pH 7.4, 150 mmol/L NaCl, and 0.1% Tween 20) and incubated overnight at 4°C with the indicated primary antibodies followed by incubation with horseradish peroxidase–tagged anti-rabbit or anti-mouse secondary antibodies for 1 hour (Promega, Abgent, cat. #W4011 and cat. #W4021, RRID: AB_430834 and RRID: AB_430833, respectively). Proteins were then visualized with the ECL system (Promega, Abgent, cat. #W4011, RRID: AB430833).

RNA-seq

After 48 hours of treatment, cells were washed with PBS and lysed in RLT Buffer provided in RNeasy Mini Kit (Qiagen). Total RNA was extracted using RNeasy Mini Kit (Qiagen) according to the manufacturer's instructions. The purified RNA samples were then sent to BGI Genomics for transcriptomic analysis.

Polyadenylated (poly-A tail) mRNA was enriched using oligo(dT) beads to selectively capture mature transcripts. The purified RNA was then fragmented, and first-strand cDNA synthesis was performed using random N6 primers for reverse transcription. Subsequently, second-strand cDNA synthesis was carried out using dUTP incorporation. The resulting cDNA underwent end-repair and 3′-adenylation, followed by adapter ligation to the 3′ ends. To ensure strand specificity, the dUTP-labeled second strand was selectively degraded using uracil-DNA glycosylase. The remaining first-strand cDNA was then PCR-amplified to generate a sequencing-ready library. The PCR product was denatured by heat, and the resulting single-stranded DNA was cyclized using a splint oligonucleotide and DNA ligase. Finally, the prepared cDNA libraries were sequenced using the DNBSEQ platform (DNBSEQ Technology).

Raw reads were filtered using SOAPnuke software developed by BGI Genomics to remove the adapter, low-quality reads, and reads whose N content is greater than 1%. Genome build/assembly: After quality control, the filtered reads were aligned to the human reference genome (*Homo sapiens*_GCF_000001405.38, GRCh38.p12) using HISAT, a splice-aware aligner optimized for RNA-seq data.

qPCR experiments

One μg of total RNA was used for the reverse transcription, using QuantiTect Reverse Transcription Kit (QIAGEN), with a mix of oligo(dT) and random primers to prime first-strand synthesis (**Table 1**). SYBR MasterMix Plus (Eurogentec) was used for qPCR. The mRNA level was normalized to *36B4* mRNA.

Colony formation assay

The cells were seeded (500 cells per condition) in dishes of diameter 60 mm and treated or not with sunitinib (0.5 μmol/L) and/or NCT-503 (30 μmol/L). Colonies were detected after 10 days of culture. Cells were then washed, fixed, and colored at room temperature for 20 minutes with crystal violet. Then, the colony area was measured by ImageJ. Three different experiments were performed.

Table 1. Primers used.

Gene name	Species	Oligonucleotide sequence (5′–3′)
ATF4	*Homo sapiens*	Forward ATGACCGAAATGAGCTTCCTG
		Reverse GCTGGAGAACCCATGAGGT
PHGDH	*Homo sapiens*	Forward CTGCGGAAAGTGCTCATCAGT
		Reverse TGGCAGAGCGAACAATAAGGC
PSAT1	*Homo sapiens*	Forward TGCCGCACTCAGTGTTGTTAG
		Reverse GCAATTCCCGCACAAGATTCT
PSPH	*Homo sapiens*	Forward GAGGACGCGGTGTCAGAAAT
		Reverse GGTTGCTCTGCTATGAGTCTCT
SHMT1	*Homo sapiens*	Forward CTGGCACAACCCCTCAAAGA
		Reverse AGGCAATCAGCTCCAATCCAA
SHMT2	*Homo sapiens*	Forward CCCTTCTGCAACCTCACGAC
		Reverse TGAGCTTATAGGGCATAGACTCG
RPLP0	*Homo sapiens*	Forward CAGATTGGCTACCCAACTGTT
		Reverse GGCCAGGACTCGTTTGTACC

Scratch assay/migration assay

The cells were seeded in 12-well plates (180,000 cells per condition). Twenty-four hours later, each well was artificially wounded by scratching the cell monolayer with a 20-μL plastic pipette tip. Images of the scratch wounds were taken 16 hours after wounding, and the measured wound width was subtracted from the wound width at time zero to obtain the net wound closure. The wound closure areas were measured with ImageJ (RRID: SCR_003070). The experiments were repeated at least 3 times.

Spheroid formation and invasion assay

For spheroid generation, 500 μL/well of cell suspensions at 10,000 cells/well were dispensed into agar-coated 24-well plates (1.5% of agarose). After 3 days of spheroid initiation, siRNA transfection was performed (25 nmol/L of siControl or siPSAT1), and 1 day later, spheroids were included in Matrigel (1 mg/mL), and 500 μL of DMEM with 7% FCS were added on the top. For NCT-503 (30 μmol/L) and sunitinib (2.5 μmol/L), treatments were performed on the day of inclusion in Matrigel both in the Matrigel and in the media on the top.

To follow invasion, area invasion was measured at different days (0, 3, and 7 days).

Metabolite profiling for targeted steady-state and flux analyses

As previously described (28), to determine the relative abundances of intracellular metabolites, extracts were prepared and analyzed by LC-MS/MS. Briefly, for targeted steady-state samples, metabolites were extracted on dry ice with 4 mL 80% methanol (−80°C), as described previously (29, 30). Insoluble material was pelleted by centrifugation at 3,000 *g* for 5 minutes, followed by two consecutive extractions of the insoluble pellet with 0.5-mL 80% methanol, with centrifugation at 20,000 *g* for 5 minutes. The 5-mL metabolite extract from the pooled supernatants was dried down under nitrogen gas using a N-EVAP device (Organomation, Inc., Associates). Fifty percent acetonitrile was added to the samples for reconstitution, followed by vortexing for 30 seconds. The sample

solution was centrifuged at 20,000 *g* for 30 minutes at 4°C. The supernatant was collected for LC-MS analysis. For isotope tracing experiments, cells were seeded in biological triplicate (~80% confluent), washed once with serum-free DMEM, and then incubated in glucose-deprived DMEM (US Biological, D9800-02) containing 25 mmol/L of $^{13}C_6$-glucose (Cambridge Isotope Laboratories, CLM-8367-PK) for 16 hours, and metabolites were extracted. For both steady-state and tracing experiments, samples were analyzed by high-performance liquid chromatography and high-resolution mass spectrometry and tandem mass spectrometry. In detail, the LC-MS/MS system is comprised of a Thermo Q-Exactive instrument in line with an electrospray ionization source and an UltiMate 3000 (Thermo Fisher Scientific) series high-performance liquid chromatography system consisting of a binary pump, degasser, and autosampler outfitted with a XBridge amide column (Waters; dimensions of 2.3 × 100 mm and a 3.5 µm particle size). The mobile phase A contained 95% (vol/vol) water, 5% (vol/vol) acetonitrile, 10 mmol/L ammonium hydroxide, and 10 mmol/L ammonium acetate, pH = 9.0; phase B was 100% acetonitrile. The gradient was as follows: 0 minutes, 15% A; 2.5 minutes, 30% A; 7 minutes, 43% A; 16 minutes, 62% A; 16.1 to 18 minutes, 75% A; and 18 to 25 minutes, 15% A with a flow rate of 150 µL/minute. The capillary of the electrospray ionization source was arranged for 275°C, with sheath gas at 35 arbitrary units, auxiliary gas at 5 arbitrary units, and the spray voltage at 4.0 kV. In positive/negative polarity switching mode, an *m*/*z* scan range from 60 to 900 was chosen, and MS1 data were collected at a resolution of 70,000. The automatic gain control target was set at 1×10^6, and the maximum injection time was 200 ms. The top 5 precursor ions were then fragmented, in a data-dependent manner, using the higher energy collisional dissociation cell set to 30% normalized collision energy in MS2 at a resolution power of 17,500. Besides matching m/z, metabolites are identified by matching either retention time with analytical standards and/or MS2 fragmentation pattern. Data acquisition and analysis were carried out by Xcalibur 4.1 software and TraceFinder 4.1 software, respectively (both from Thermo Fisher Scientific). Metabolomic pathway analysis was calculated using MetaboAnalyst software (https://www.metaboanalyst.ca/; ref. 31).

Ectopic model of RCC

Five million 786-O cells were injected subcutaneously into the flank of 5-week-old nude (nu/nu) female mice (Janvier). The tumor volume was determined using a caliper ($v = L \times l^2 \times 0.5$). When the tumor reached 100 mm^3, mice were treated 5 days a week for 4 weeks by gavage with placebo (dextrose water vehicle) or sunitinib (40 mg/kg). This study was carried out in strict accordance with the recommendations in the Guide for the Care and Use of Laboratory Animals.

siRNA assay

Cells were transfected with either 25 nmol/L of siPSAT1 (SMARTpool, Dharmacon) or siControl (SMARTpool, Dharmacon) by transfection with Lipofectamine RNAiMAX (Invitrogen) in Opti-MEM.

Enzymatic dissociation of primary RCC cells

Tissue dissection followed by enzymatic digestion (DNase, collagenase, and dispase, 37 degrees, 30 minutes) and mechanical dissociation were performed to obtain single-cells culture of primary RCC cells. Cells were then grown with PromoCell Renal Epithelial Cell Growth Medium 2 (PromoCell).

Gene expression microarray analysis

Normalized RNA-seq data produced by The Cancer Genome Atlas (TCGA) were downloaded from cBiopotal (www.cbioportal.org, TCGA provisional; RNA-seq V2). Data were available for 538 RCC tumor samples TCGA subjected to mRNA expression profiling (Firehose legacy). The Kaplan–Meier method was used to produce overall survival and progression-free survival curves.

Zebrafish tumor model

All animal experiments were conducted with approval from the Northern Stockholm Experimental Animal Ethical Committee. Zebrafish embryos of the transgenic strain expressing enhanced GFP under the Fli1 promoter (Fli1:EGFP, RRID: ZIRC_ZL1405) were raised at 28°C under standard experimental conditions. Zebrafish embryos at the age of 24 hours post-fertilization (hpf) were incubated in aquarium water containing 0.2 mmol/L 1-phenyl-2-thiourea (Sigma-Aldrich). At 48-hpf, Fli1:EGFP zebrafish embryos were dechorionated using a pair of sharp-tip forceps and anesthetized with 0.04 mg/mL of tricaine (MS-222, Sigma-Aldrich). Anesthetized embryos were subjected for microinjection. 786-0 cells were labeled *in vitro* with 2 µg/mL of Vybrant DiD cell-labeling solution (Life Technologies). The labeled cells were resuspended in DMEM with 2 mmol/L of EDTA, and 5 nL of the cell solution were injected into the perivitelline space of each embryo using an Eppendorf microinjector (FemtoJet 5247, Eppendorf and Manipulator MM33-Right, Märzhäuser Wetziar). Nonfilamentous borosilicate glass capillary needles were used for injection, and the injected zebrafish embryos were immediately transferred into 1-phenyl-2-thiourea aquarium water. Injected zebrafish embryos were monitored 48 hours to assess tumor cell invasion and metastasis using a fluorescent microscope (Nikon Eclipse C1, RRID: SCR_009921).

Generation of PSAT1 knockout via CRISPR-Cas9

The selected guide RNA (gRNA) target regions were designed using the ChopChop web tool (RRID: SCR_015723; ref. 32). The following gRNA guides are used in this study:

CrPSAT1_ex6 GTCATCACGGACAATCACCA (#5)
CrPSAT1_ex6 GACCTTGTATTCCAGGACCGA (#17)
CrPSAT1_ex2 GACTCAGTAAGTCCCCGCGAG (#6)

Bold G in 5′ is added due to the transcription initiation requirement of a "G" base for the human U6 promoter. 786-O wild-type cells were transfected using PEI (Polyplus transfection) with pSpCas9(BB)-2A-GFP (PX458) plasmids (a gift from Feng Zhang (plasmid #48138, Addgene, RRID: Addgene_48138; ref. 33) containing CRISPR-Cas9 and gRNA.

As the pSpCas9(BB)-2A-GFP (pX458) plasmid used in the study contains GFP, single-cell sorting was conducted (24-hour after transfection) using BD FACSMelody (BD Biosciences, RRID: SCR_023209). Individual clones were cultivated in DMEM with 7% FBS. Each individual clone was analyzed for PSAT1 expression by qRT-PCR and immunoblotting.

Statistical analysis

One-way ANOVA followed by the Tukey *post hoc* test were performed in GraphPad Prism 7.0 to determine differences between each group when more than two conditions were present. A two-tailed Student *t* test was performed for two pairwise comparisons. All error bars represent the SD. A value of $P < 0.05$ was considered significant.

Data availability

Raw RNA-seq data for this study were generated at BGI Genomics and are no longer available. Derived RNA-seq data supporting the findings of this study are provided in Supplementary Table S1. The data analyzed from TCGA are available on http://www.cbioportal.org/study/summary?id=kirc_tcga [Kidney Renal Clear Cell Carcinoma (TCGA, Firehose Legacy; 538 samples)]. All other raw data are available upon request from the corresponding author.

Results

Sunitinib leads to an upregulation of the serine biosynthesis pathway in ccRCC cells

To investigate the transcriptional alterations induced by sunitinib in ccRCC, we treated 786-O renal cancer cells with a suboptimal concentration of sunitinib for 48 hours, followed by RNA-seq. The plasma concentrations of patients or mice exposed to sunitinib is low (0.1–1 μmol/L range) compared with the intratumor amount, which was 10 times higher (10 μmol/L range). The IC_{50} value of mRCC cells is approximately 5 μmol/L (34, 35). In the presence of a concentration of sunitinib below the IC_{50} value (2.5 μmol/L), as we previously observed (13), mRCC cells have a reduced proliferation rate. A suboptimal concentration of sunitinib (2.5 μmol/L) did not affect cell viability, whereas exposure to a higher concentration resulted in cell death, as measured by cell counting (Supplementary Fig. S1A and S1B). This experimental design ensures that the metabolic changes observed are a direct result of the effects of sunitinib on cellular processes rather than secondary effects of cell death.

RNA-seq identified 283 downregulated and 478 upregulated transcripts in sunitinib-treated cells (Supplementary Fig. S2A). To further understand the functional implications of these differentially expressed genes, we conducted gene set enrichment analysis and utilized gene ontology terms alongside the Kyoto Encyclopedia of Genes and Genomes pathway analysis (Supplementary Fig. S2B). Sunitinib treatment led to a significant enrichment of multiple Kyoto Encyclopedia of Genes and Genomes pathways, including glycine, serine, and threonine metabolism, PI3K-Akt signaling, p53 signaling, lysosome, and cell-cycle pathways (**Fig. 1A**; Supplementary Fig. S2C). The glycine, serine, and threonine pathway was consistently enriched across both 786-O and A498 RCC cells (Supplementary Fig. S2D).

To determine whether changes in metabolic gene expression correlated with alterations at the metabolite level, we conducted targeted metabolomic analysis on parental 786-O cells, sunitinib-sensitive 786-O cells, and sunitinib-resistant 786-O cells, all treated with either vehicle or sunitinib (Supplementary Fig. S3A and S3B). Interestingly, the metabolic profiles of sunitinib-resistant cells treated with vehicle were largely unchanged upon sunitinib treatment, suggesting these cells had adapted metabolically to prolonged sunitinib exposure (**Fig. 1B** and **C**). Pathway impact analysis highlighted glycine, serine, and threonine metabolism as one of the most upregulated networks in both sunitinib-sensitive (**Fig. 1D**; Supplementary Fig. S3A; impact factor ≥ 0.1) and -resistant cells (**Fig. 1E**; Supplementary Fig. S3B; impact factor ≥ 0.1). Importantly, sunitinib treatment led the accumulation of serine biosynthesis intermediates, such as 3-phosphohydroxypyruvate and serine, particularly in sunitinib-resistant cells (**Fig. 1F**). On the other hand, extracellular serine and glycine levels remained unchanged across all conditions, indicating that the upregulation of serine biosynthesis was an intracellular adaptation (**Fig. 1G**).

Proliferating cells synthesize serine from the glycolytic intermediate 3-phosphoglycerate through a three-step enzymatic process, involving PHGDH, PSAT1, and PSPH (**Fig. 2A**; refs. 36, 37). In our study, sunitinib-resistant cells exhibited a significant increase in both serine levels and the serine/3-phosphoglycerate ratio, indicating enhanced serine biosynthesis (**Fig. 2B** and **C**). Stable isotope tracing using [$^{13}C_6$]-glucose confirmed an elevated rate of serine synthesis in sunitinib-treated 786-O cells compared with vehicle-treated 786-O cells (**Fig. 2D**). The acute [$^{13}C_6$]-glucose tracing experiment showed that most intracellular serine was unlabeled and only a small fraction contained the M+3 label, consistent with the typical dynamics of metabolic tracing under acute labeling. Despite the limited enrichment, the results provide valuable insight into the activity of serine synthesis in ccRCC cells (Supplementary Fig. S3C).

Further analysis revealed that *PHGDH*, *PSPH*, and *PSAT1* mRNA expression increased following both short-term sunitinib treatment and chronic exposure compared with untreated controls (**Fig. 2E**). The increase of *PSAT1* and *PSPH* mRNA expression under sunitinib treatment and in resistant cells was confirmed at the protein levels, but PHGDH protein levels remained unchanged (**Fig. 2F**; Supplementary Fig. S4A).

Similarly, cytosolic *SHMT1* and mitochondrial *SHMT2*, which convert serine to glycine and generate one-carbon units, showed increased mRNA levels but no changes at the protein levels in 786-O cells (Supplementary Fig. S4B and S4C).

These findings were consistent in RCC10 cells, in which we observed similar patterns of upregulation for *PHGDH*, *PSPH*, *PSAT1*, *SHMT1*, and *SHMT2* (Supplementary Fig. S5A–S5C).

Overall, these gene expression and metabolic profiles reveal an upregulation of the serine synthesis pathway in renal cancer cells in response to sunitinib treatment, underscoring the critical role of transcriptional regulation and metabolic adaptation in the development of sunitinib resistance in ccRCC.

The ISR pathway is required for sunitinib-dependent induction of *de novo* serine synthesis

Amino acid and glucose deprivation, along with the generation of reactive oxygen species, which are common stress factors in solid tumors, activate the eukaryotic initiation factor 2α (eIF2α)-kinase GCN2 (38–40). Once activated, GCN2 phosphorylates eIF2α, leading to the translational upregulation of activating transcription factor 4 (ATF4; refs. 41, 42). ATF4 is the main transcription factor known to directly bind the promoter of serine synthesis genes, subsequently promoting their expression (43, 44). Upon conditions such as amino acid starvation, eIF2α phosphorylation reduces global protein synthesis but selectively enables the translation of certain genes, including ATF4, facilitating metabolic adaptation and cell survival (41, 42, 45).

The ISR pathway was activated within 30 minutes of sunitinib treatment in 786-O cells, evidenced by increased phosphorylation of GCN2, eIF2α, and induction of ATF4 (**Fig. 3A** and **B**). As a control, we induced ISR with tunicamycin, yielding similar effects on the eIF2α–ATF4 axis and increasing PSAT1 and PSPH protein levels (**Fig. 3B**). The regulation of GCN2–eIF2α and the increase in serine levels upon both sunitinib and tunicamycin conditions in sensitive or resistant cells (**Fig. 3C**) highlight the canonical induction of ISR under these conditions. To determine whether GCN2 and ATF4 are required for increased serine synthesis enzymes under sunitinib treatment, we suppressed *GCN2* (**Fig. 3D**) or *ATF4* (**Fig. 3E**) expression using siRNA. Knockdown of *GCN2* or *ATF4* prevented the sunitinib-dependent increase in PSAT1 and PSPH

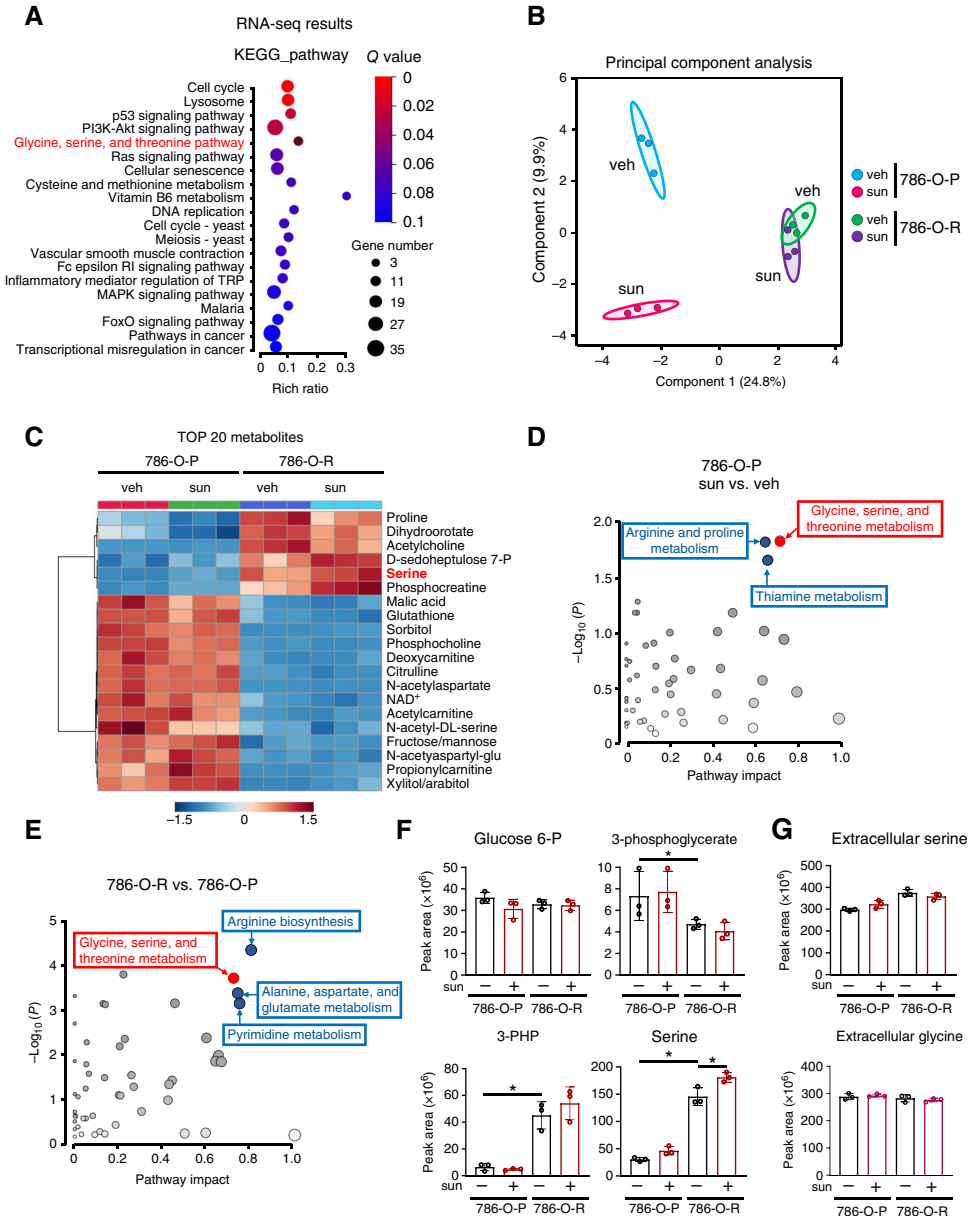

Figure 1.

Metabolic reprogramming and increased serine metabolism in sunitinib-treated ccRCC. **A,** Functional enrichment analysis based on Kyoto Encyclopedia of Genes and Genomes (KEGG) pathways presented as dot–bubble plots. Pathways are ordered by ascending significance, comparing sunitinib-treated 786-O parental cells with control (vehicle-treated) cells. Bubble size is proportional to the impact of each pathway, with the most significantly altered pathways characterized by a high −log(*P*) value and high pathway impact (top right region). Glycine, serine, and threonine metabolism are highlighted in red. **B,** Steady-state metabolite profiles of 786-O cells treated with DMSO (veh) or sunitinib (sun; 2.5 μmol/L, 15 hours). The heatmap shows the top 20 significantly altered metabolites, measured by LC-MS/MS, line-normalized, and ranked by *P* value. Data include 786-O parental (786-O-P) and sunitinib-resistant (786-O-R) cells, each condition represented by biological triplicates. **C,** Dendrogram illustrating the steady-state metabolomic analysis conducted in triplicate for three conditions: control (veh), sunitinib-treated cells (sun), and cells resistant to sunitinib not treated (R) or treated (R +sun) with sunitinib. The vertical axis represents the complexes analyzed as samples, whereas the horizontal axis indicates the average distance between different clusters. **D,** Bubble plots depict altered metabolic pathways in 786-O parental cells treated with sunitinib (786-O-P +sun) compared with DMSO (veh). **E,** Bubble plots illustrate the differences in altered metabolic pathways between sunitinib-resistant cells (786-O R) and parental cells (786-O-P). **F,** Normalized peak areas of various metabolites serving as intermediates in the serine biosynthesis pathway are presented to provide insights into the impact of sunitinib treatment and resistance mechanisms. **G,** Normalized peak areas of extracellular serine in 786-O parental cells (786-O-P) or 786-O resistant cells (786-O-R) treated with sunitinib (+) compared with DMSO (−). Glucose-6-P, glucose-6-phosphate; 3-PHP, 3-phospho-hydroxypyruvate. *, $P < 0.05$ (two-way ANOVA).

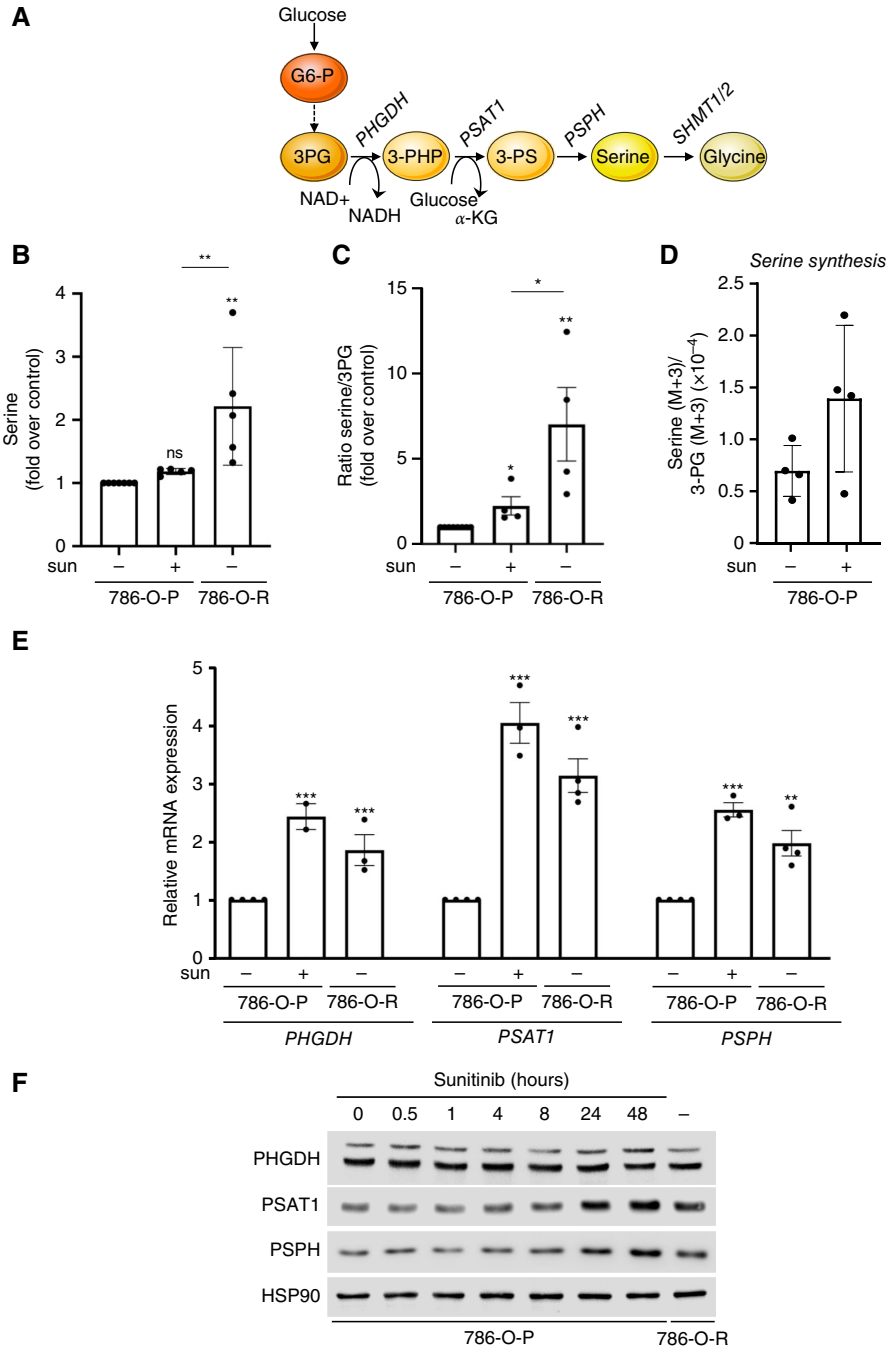

Figure 2.

Treatment with sunitinib leads to increased serine biosynthesis *in vitro*. **A,** Schematic of the serine biosynthesis pathway and the enzymes directly involved and associated with this pathway. **B,** Serine levels measured in parental 786-O cells (786-O-P) and sunitinib-resistant cells (786-O-R). Cells were treated with vehicle (DMSO) or sunitinib (sun; 2.5 μmol/L, 48 hours), and normalized peak areas of serine were quantified via LC-MS/MS from five independent steady-state experiments. Data are presented as fold change relative to the control (vehicle-treated 786-O-P cells). **C,** Ratio of serine to 3PG measured from four independent steady-state experiments in parental RCC cells (786-O-P) treated with vehicle (DMSO) or sunitinib (2.5 μmol/L, 48 hours) and in sunitinib-resistant RCC cells (786-O-R). Data are presented as fold change over control. **D,** Ratio of serine (M+3) to 3-phosphoglycerate (3PG; M+3) based on two independent flux experiments in parental RCC cells (786-O-P) treated with vehicle or sunitinib (2.5 μmol/L, 48 hours). Cells were incubated in [$^{13}C_6$]-glucose–containing medium for 15 hours, and the synthesis of serine from glucose was measured by LC-MS/MS. **E,** Relative mRNA expression levels of PHGDH, PSAT1, and PSPH in parental RCC cells (786-O-P) treated with vehicle (DMSO) or sunitinib (2.5 μmol/L, 48 hours) and in sunitinib-resistant cells (786-O-R). The mRNA levels were quantified by qPCR and normalized to control levels. Data represent the mean of three to four independent experiments. **F,** Immunoblots of parental RCC cells (786-O-P) treated with sunitinib (2.5 μmol/L) for the indicated time points and in sunitinib-resistant RCC cells (786-O-R). ns, nonsignificant; *, $P < 0.05$; **, $P < 0.01$; ***, $P < 0.001$ (two-way ANOVA).

protein levels. Consistent with these findings, labeling experiments with ^{15}N-(amine)-glutamine revealed that sunitinib treatment significantly increased 3-phosphoserine (M+1) abundance in 786-O cells, whereas *ATF4* knockdown effectively reduced this increase, highlighting the critical role of ATF4 in regulating serine synthesis (Supplementary Fig. S6A and S6B). In contrast, no changes were observed on SHMT1 and SHMT2 protein levels upon sunitinib treatment and *ATF4* knockdown (Supplementary Fig. S6C). In our model, we propose that the GCN2–eIF2α pathway is required to mediate the sunitinib-dependent induction of ATF4 expression. ATF4 translation is typically induced by the phosphorylation of eIF2α, a process reliant on upstream open reading frames in the 5' untranslated region of the *ATF4* transcript (46). Through cycloheximide protein stability assay, we showed that sunitinib treatment, similarly to tunicamycin, increased ATF4 protein stability in 786-O cells (Supplementary Fig. S6D).

Whereas mTORC1 signaling has been shown to control ATF4 protein levels independently of the canonical ISR pathway (47,48), rapamycin treatment did not prevent the induction of ATF4 expression in response to sunitinib. Similarly, inhibition of

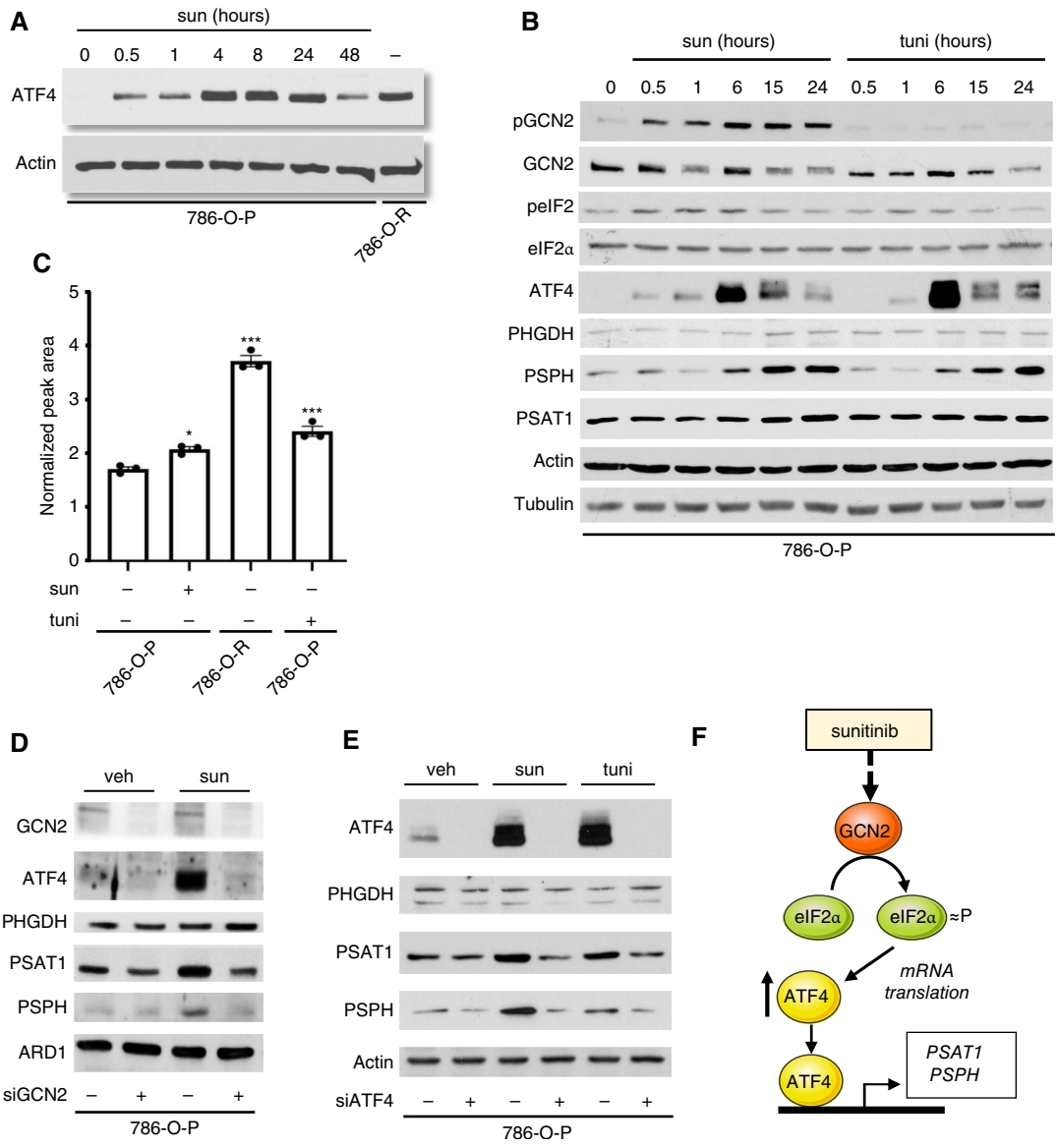

Figure 3.

The GCN2/eIF2/ATF4 RE stress response pathway is required for activation of the serine biosynthesis pathway. **A,** Immunoblots showing ATF4 protein expression in parental RCC cells (786-O-P) treated with DMSO (vehicle) or sunitinib (sun; 2.5 μmol/L) for the indicated time points (0–48 hours) and in sunitinib-resistant cells (786-O-R). **B,** Immunoblots of 786-O-P cells treated with sunitinib (2.5 μmol/L) or tunicamycin (tuni; 1 μg/mL) for the indicated time points. **C,** Normalized peak areas of serine from steady-state metabolite profiling in 786-O-P cells treated with DMSO (veh), sunitinib (2.5 μmol/L), or tunicamycin (1 μg/mL) and in sunitinib-resistant cells (786-O-R). Three different experiments were conducted. **D,** Immunoblots of 786-O-P cells treated with DMSO (veh) or sunitinib (2.5 μmol/L) for 48 hours, following transfection with siGCN2 or control siRNA. **E,** Immunoblots of 786-O-P cells treated with DMSO (veh), sunitinib (2.5 μmol/L), or tunicamycin (1 μg/mL), following transfection with siATF4 or control siRNA. **F,** Schematic diagram depicting the mechanism by which sunitinib induces the ISR pathway. Sunitinib activates GCN2, leading to phosphorylation of eIF2α, which enhances ATF4 translation. ATF4 then upregulates serine biosynthesis enzymes, PSAT1 and PSPH, to sustain cellular metabolism under stress. *, $P < 0.05$; ***, $P < 0.001$ (two-way ANOVA).

PKC (GF109203X, GFX) or ERK (U0126) did not avert the induction of ATF4 upon sunitinib treatment (Supplementary Fig. S6E). Therefore, mTORC1, PKC, and ERK do not contribute to the sunitinib-dependent regulation of ATF4, suggesting that the regulation of ATF4 upon sunitinib treatment is independent of the molecular mechanisms involved in growth factor–dependent control of ATF4 expression.

Consistent results were observed in RCC10 cells under sunitinib treatment, confirming the activation of the GCN2–eIF2α–ATF4 pathway (Supplementary Fig. S7A). ATF4, PSAT1, and PSPH protein levels were also increased in RCC10 cells treated with tunicamycin (Supplementary Fig. S7B). The role of ATF4 in regulating PSAT1 and PSPH, but not PHGDH, was confirmed using siRNA in RCC10 cells (Supplementary Fig. S7B). In summary, the increased

serine synthesis following sunitinib treatment necessitates the activation of the ISR pathway GCN2–eIF2α–ATF4, which orchestrates the expression of key serine synthesis enzymes (**Fig. 3F**).

The induction of the *de novo* serine pathway upon sunitinib treatment supports cell proliferation and nucleotide synthesis

To understand whether the synthesis of serine serves as a metabolic mechanism enabling RCC cells to resist sunitinib treatment, we used NCT-503 (19), an inhibitor of PHGDH, the rate-limiting enzyme of *de novo* serine synthesis. The combination of sunitinib and NCT-503 significantly reduced the proliferation of both sunitinib-sensitive and -resistant RCC cells, surpassing the efficacy of individual treatments (**Fig. 4A**). To further validate these observations, we utilized a genetic approach using siRNA targeting either *PHGDH*, *PSAT1*, or *PSPH* within the serine synthesis pathway in the presence or absence of sunitinib. Knockdown of *PSPH* in combination with sunitinib exhibited the most striking decrease in RCC cell number compared with the knockdown of other serine synthesis genes (**Fig. 4B**).

Furthermore, a colony formation assay revealed a notable reduction in colony formation when sunitinib-sensitive or -resistant cells were cotreated with sunitinib and NCT-503, as opposed to single treatments (**Fig. 4C**). These effects were further validated in RCC10 cells, supporting the critical role of serine synthesis in maintaining cell proliferation in both sunitinib-sensitive and -resistant RCC cells under sunitinib treatment (Supplementary Fig. S7C). These results suggest potential therapeutic strategies involving the inhibition of this pathway to enhance the efficacy of ccRCC treatment.

To better understand the mechanisms underlying the observed growth inhibition, we conducted metabolite profiling of RCC cells treated with vehicle, sunitinib, NCT-503, or both sunitinib and NCT-503. This analysis revealed that nucleotides were among the most significantly depleted metabolites when sunitinib and the PHGDH inhibitor were combined (Supplementary Fig. S8A). These results suggest that nucleotide synthesis is further compromised under combined treatment, which may contribute to the decreased cell proliferation.

Considering the role of serine as substrate for nucleotide synthesis, we hypothesize that RCC cells resist sunitinib treatment by sustaining *de novo* nucleotide synthesis through serine synthesis stimulation. To investigate the impact of sunitinib on the metabolic flux of newly synthesized nucleotides into nucleic acids, we measured the incorporation of carbon from U-[^{14}C]-glucose into RNA. Whereas sunitinib alone reduced the incorporation of ^{14}C from glucose into RNA, the combination of sunitinib and NCT-503 resulted in a further decrease in ^{14}C incorporation into RNA in both sensitive and resistant cells compared with NCT-503 or sunitinib treatment alone (**Fig. 4D**).

To directly assess nucleotide synthesis activity, we conducted a [^{15}N-amide]-glutamine tracing experiment, as glutamine is a key substrate in the nucleotide synthesis pathway (Supplementary Fig. S8B). Our results demonstrate that sunitinib treatment led to a decreased abundance of inosine monophosphate (M+2), the first purine nucleotide formed in the pathway (Supplementary Fig. S8C). Importantly, inosine monophosphate (M+2) levels were further reduced when sunitinib was combined with the PHGDH inhibitor (Supplementary Fig. S8C), indicating that the combination treatment more effectively limits *de novo* nucleotide synthesis (Supplementary Fig. S8C and S8D). Collectively, these findings demonstrate that sunitinib reduces nucleotide synthesis, but combining it with a PHGDH inhibitor further exacerbates this effect, thereby limiting the metabolic resources necessary for RCC cell proliferation and survival.

The induction of the *de novo* serine pathway upon sunitinib treatment supports cell migration and invasion

Whereas numerous studies associate serine biosynthesis with tumor growth, limited attention has been given to its role in migration, invasion, and metastasis, with existing studies mainly focused on breast cancer (49, 50). To assess the effects of serine synthesis on ccRCC migration, invasion, or metastasis, we used siRNA to reduce PSAT1 expression or utilized a PHGDH inhibitor (NCT-503) to inhibit PHGDH activity in ccRCC cells treated with either vehicle or sunitinib. We performed wound-healing assays to address migration and spheroids invasion assays to address invasion.

In our wound-healing assays, we observed that *PSAT1* knockdown significantly decreased the motility of 786-O cells, with no discernible difference in sunitinib-treated cells compared with those treated with vehicle. Strikingly, the antimigratory effects of *PSAT1* knockdown were more pronounced in sunitinib-resistant cells than in vehicle-treated parental cells with reduced PSAT1 expression (**Fig. 5A**).

PHGDH inhibition with NCT-503 or suppression of PSAT1 with siRNA significantly reduced the invasive ability of spheroid RCC cells, with a more pronounced effect when combined with sunitinib (**Fig. 5B** and **C**). However, this more pronounced effect was not observed in sunitinib-resistant cells. Interestingly, spheroids of sunitinib-resistant RCC cells showed increased sensitivity to PHGDH inhibition under serine-deprived condition (**Fig. 5D**), suggesting that serine availability is also essential for the invasive capacity of resistant cells. In parental 786-O cells, serine deprivation alone reduced invasive potential, and the combination with either sunitinib or NCT-503 intensified this effect (Supplementary Fig. S9A). These findings indicate that whereas parental cells rely on extracellular serine for invasion, resistant cells maintain invasive potential even in the absence of extracellular serine (Supplementary Fig. S9B). This suggests that resistant cells adapt to utilize intracellular serine when extracellular serine levels are low. On the contrary, when serine biosynthesis is inhibited, resistant cells are likely to readily rely on extracellular serine, whereas parental cells are more impacted. Overall, these results suggest a critical role of both intracellular and extracellular serine sources in regulating invasion and resistance behaviors of RCC cells.

Sunitinib treatment promotes *de novo* serine synthesis across diverse cancer models

Given that sunitinib primarily targets receptor tyrosine kinases such as VEGFR2, PDGFRβ, or c-KIT, which are known to be activated in various cancers (51), we aimed to broaden our investigation into the effects of sunitinib on serine metabolism across others cancer cell lines. These included BT-549 (TNBC), A549 (lung cancer), DAOY (medulloblastoma), and CAL33 (head and neck cancer). Consistent with our findings in RCC cells, sunitinib treatment led to an increase in protein levels of serine synthesis enzymes (**Fig. 6A**). This indicates that the induction of the serine biosynthetic pathway is not limited to ccRCC but extends to diverse tumor types. Similarly to the strategies used in ccRCC, we inhibited *de novo* serine synthesis with the PHGDH inhibitor NCT-503 in these cancer cell lines. Combining sunitinib with NCT-503 resulted in a significant decrease in proliferation after 4 days compared with

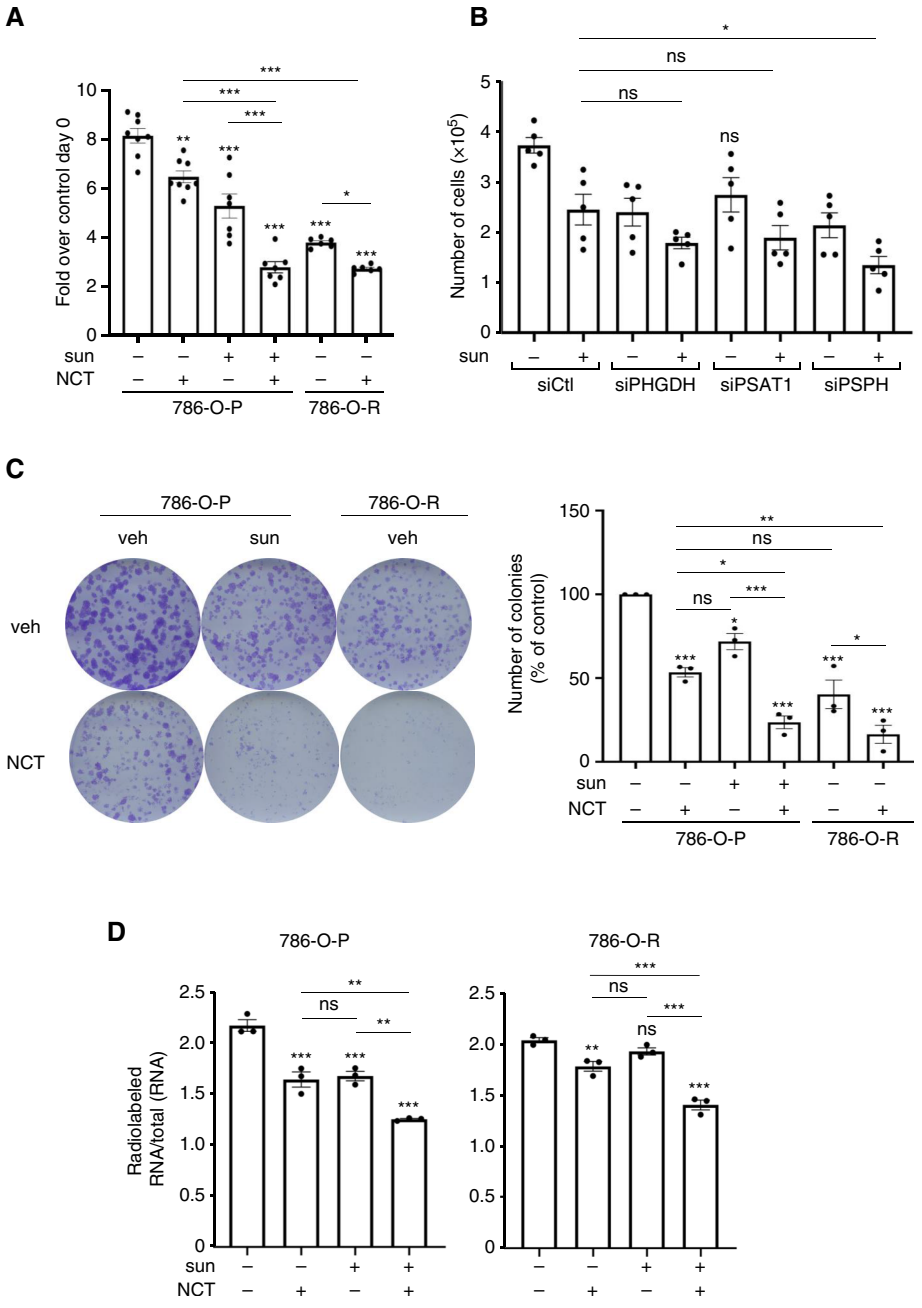

Figure 4.

The *de novo* serine synthesis pathway is essential for proliferation and nucleotide synthesis under sunitinib treatment. **A,** Cell proliferation assay measured by CellTiter-Glo in 786-O parental (786-O-P) and sunitinib-resistant (786-O-R) cells 96 hours after treatment with vehicle (DMSO), sunitinib (sun; 2.5 μmol/L), NCT-503 (NCT; 30 μmol/L), or a combination of both treatments. Three different experiments were conducted. **B,** Cell number quantification of 786-O-P cells 96 hours after treatment with vehicle (DMSO) or sunitinib (2.5 μmol/L) after transfection with siRNAs targeting PHGDH, PSAT1, PSPH, or nontargeting pools (siCtl). Cells were counted, and five independent experiments were conducted. **C,** Clonogenic assay of 786-O-P and 786-O-R cells treated with DMSO (veh), sunitinib (2.5 μmol/L), NCT-503 (30 μmol/L), or their combination. Colonies were cultured for 10 days, photographed, and quantified using ImageJ. The number of colonies is shown as a percentage of the control. Three different experiments were conducted. **D,** Relative incorporation of radiolabeled U-[^{14}C]-glucose into total RNA in 786-O-P and 786-O-R cells treated with vehicle (DMSO), sunitinib (2.5 μmol/L), NCT-503 (30 μmol/L), or a combination of both treatments for 24 hours. Three different experiments were conducted. ns, nonsignificant; *, $P < 0.05$; **, $P < 0.01$; ***, $P < 0.001$ (two-way ANOVA).

treatment with sunitinib alone (**Fig. 6B**). These compelling results suggest that the biosynthetic pathway plays a pivotal role in sunitinib resistance, demonstrating its relevance independent of the specific tumor type.

Sunitinib treatment promotes serine biosynthesis in RCC tumors and in samples from patients with RCC

To investigate whether sunitinib stimulates the *de novo* serine pathway in tumors, we implanted 786-O cells subcutaneously into nude mice and administered sunitinib (**Fig. 7A**). Metabolite profiling showed distinct metabolic alterations in sunitinib-treated tumors compared with nontreated tumors (Supplementary Fig. S10A–S10C).

Significant changes were observed in several major metabolic pathways, including pantothenate and CoA biosynthesis; glycine, serine, and threonine metabolism; and arginine and proline metabolism. Notably, glycine, serine, and threonine metabolism stood out as the second most differentially enriched pathway in RCC tumors from sunitinib-treated mice (**Fig. 7B**; Supplementary Fig. S10C; impact factor ≥ 0.1). This was supported by steady-state metabolite profiling, which identified several differentially produced metabolites, including *de novo* serine synthesis intermediates (**Fig. 7C**; Supplementary Fig. S10B).

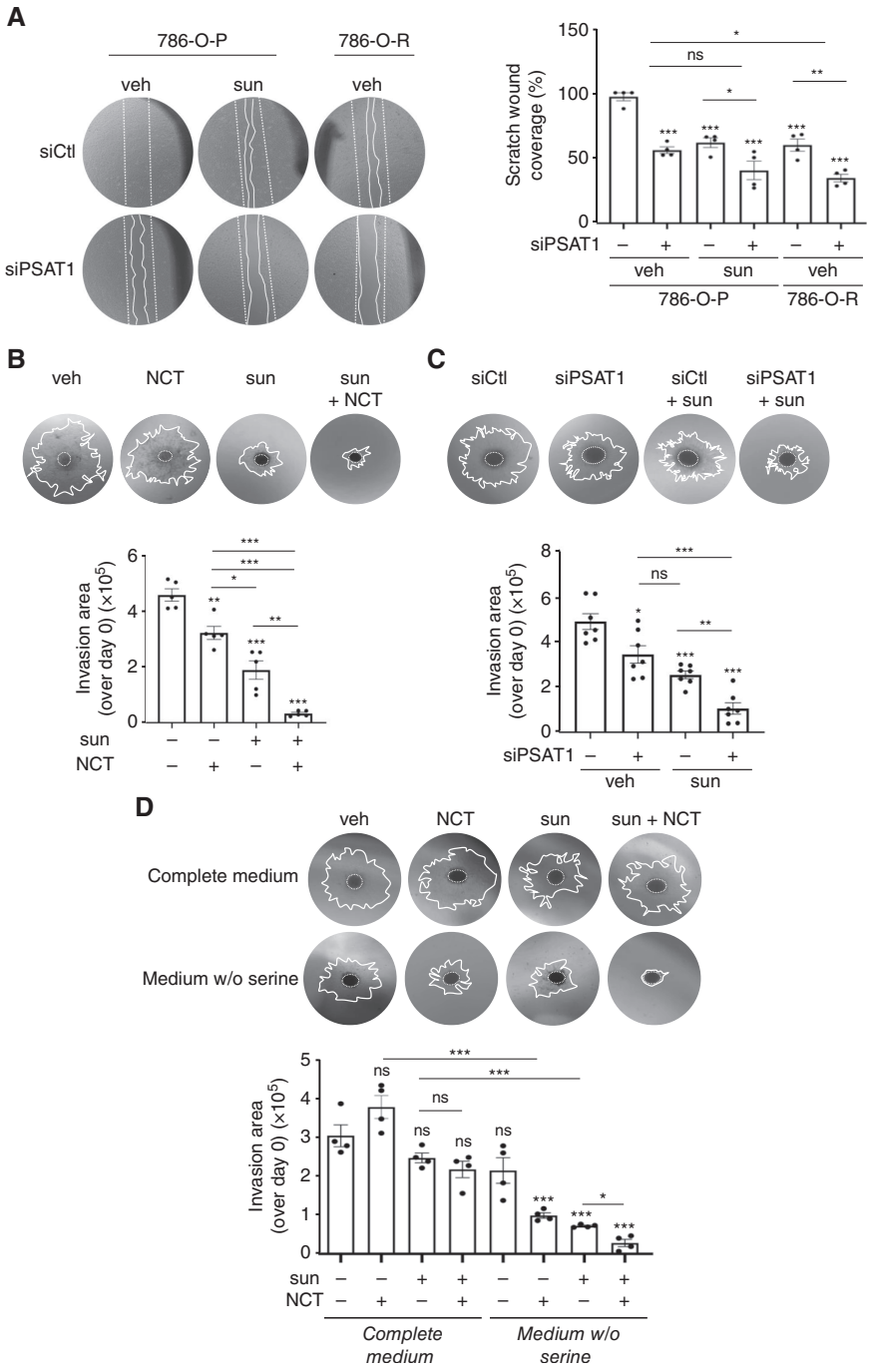

Figure 5.

The *de novo* serine synthesis pathway supports migration and invasion under sunitinib treatment. **A,** Cell migration measured by a scratch wound–healing assay in 786-O parental RCC cells (786-O-P) and sunitinib-resistant cells (786-O-R) treated with DMSO (veh) or sunitinib (sun; 2.5 μmol/L) and transfected with siRNAs targeting PSAT1 (siPSAT1) or nontargeting controls (siCtl). Quantification represents the percentage of wound closure after 16 hours. Data are presented as the mean ± SEM ($n = 4$). Four different experiments were conducted. **B,** Quantification of spheroid invasion area of 786-O-P cells after 4 days of invasion. Spheroids were treated with DMSO (veh), sunitinib (2.5 μmol/L), NCT-503 (NCT; 30 μmol/L), or their combination 24 hours before embedding in Matrigel (1 mg/mL). Three different experiments were conducted. **C,** Spheroid invasion assay of 786-O-P cells transfected with siRNAs targeting PSAT1 (siPSAT1; 25 nmol/L) or nontargeting pools (siCtl) were subsequently treated with DMSO or sunitinib (2.5 μmol/L) for 24 hours before embedding in Matrigel (1 mg/mL). Three different experiments were conducted. **D,** Spheroid invasion assay of sunitinib-resistant (786-O-R) cells treated with DMSO (veh), sunitinib (2.5 μmol/L), NCT-503 (30 μmol/L), or a combination of both. Spheroids were cultured in either complete media or serine-free media for 4 days. Two different experiments were conducted. ns, nonsignificant; *, $P < 0.05$; **, $P < 0.01$; ***, $P < 0.001$ (two-way ANOVA).

Consistent with *in vitro* results, sunitinib-treated tumors exhibited elevated levels of serine and phosphoserine (**Fig. 7C**). Analysis of mRNA expression data from TCGA indicated that high expression of *PSAT1* was associated with lower disease-free survival, progression-free survival, and overall survival in patients with renal cancer (Supplementary Fig. S11). However, no significant differences were found between patients with renal cancer with tumors expressing low or high levels of *PHGDH* and *PSPH* (Supplementary Fig. S11).

RCC tumor samples from the University Hospital of Nice in France, treated with sunitinib over time, showed rapid increases in PHGDH, PSPH, and PSAT1 protein levels. Additionally, these RCC tumor cells treated with sunitinib showed an activation of the GCN2–eIF2α axis and an increase in ATF4 protein levels (**Fig. 7D**). These results mirrored findings observed in 786-O cells, reinforcing the clinical relevance of sunitinib-induced serine biosynthesis and ISR activation in ccRCC.

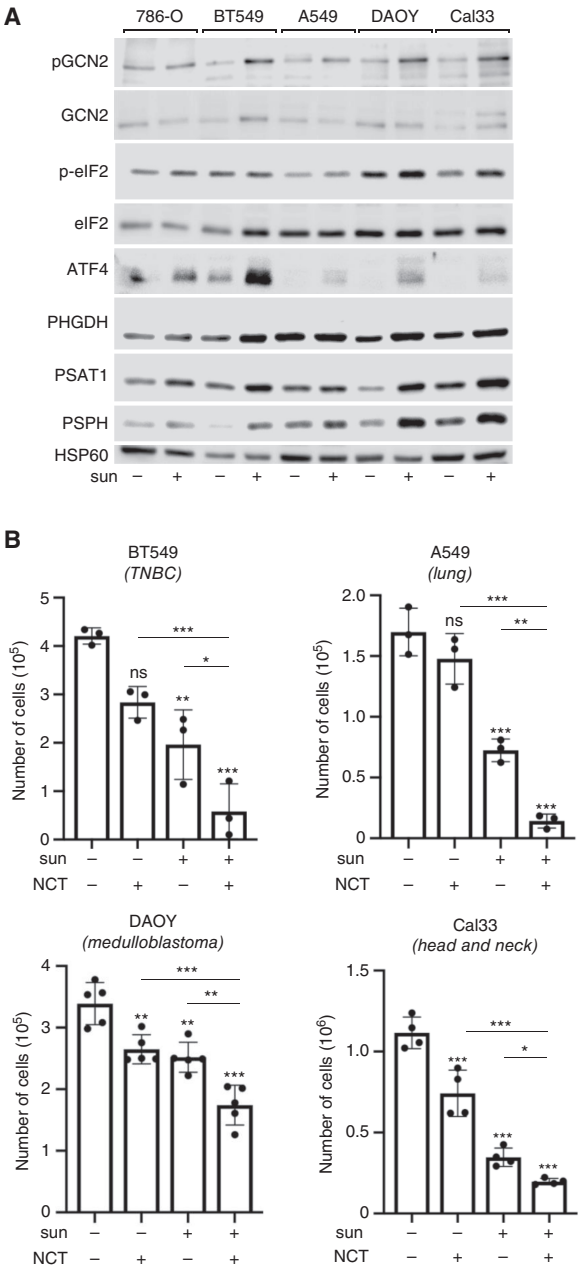

Figure 6.

Sunitinib treatment enhances *de novo* serine metabolism across multiple cancer models. **A,** Immunoblots various cancer lines, including 786-O (ccRCC), BT549 (TNBC), A549 (lung), DAOY (medulloblastoma), and Cal33 (head and neck), treated with DMSO (veh) or sunitinib (sun; 2.5 μmol/L) for 48 hours. **B,** Cell count measurements conducted 96 hours after treating BT549, A549, DAOY, and Cal33 with DMSO (veh), sunitinib (2.5 μmol/L), NCT-503 (NCT; 30 μmol/L), or a combination of both treatments. Three different experiments were conducted. ns, nonsignificant; *, $P < 0.05$; **, $P < 0.01$; ***, $P < 0.001$ (two-way ANOVA).

Moreover, combining NCT-503 with sunitinib remarkably suppressed human RCC cell proliferation more effectively than either treatment alone (**Fig. 7E**). PHGDH inhibition also markedly suppressed RCC tumor cell invasiveness (**Fig. 7F**). These findings support the concept that during sunitinib treatment, *de novo* serine synthesis emerges as a metabolic vulnerability and can be effectively targeted to combat RCC.

Inactivation of the serine synthesis pathway exhibits antitumor and antimetastasis effects in a zebrafish model

To assess the potential contribution of sunitinib-induced serine synthesis to ccRCC tumor formation and dissemination, we used a zebrafish model for cancer growth and metastasis studies (52). Utilizing 786-O cells, known for their efficient metastasis in zebrafish tails (53), we examined the tumor growth and metastatic potential of ccRCC cells with or without *PSAT1*, treated with either vehicle or sunitinib. 786-O cells, whether depleted of *PSAT1* or not, were labeled with a lipophilic dye (DiI) and injected into the perivitelline space of zebrafish embryos at 48-hpf. At 2 days after injection, we assessed the extent and growth of the tumor by measuring the tumor area and red fluorescent protein signal intensity (**Fig. 8A**). Quantification analysis revealed a significant reduction in distal metastatic tumor cells when 786-O cells lacked *PSAT1* and zebrafish were treated with sunitinib (**Fig. 8B** and **C**). Additionally, *PSAT1*-depleted cells exhibited smaller RCC tumors compared with those derived from control ccRCC cells, with further reductions observed during sunitinib treatment (**Fig. 8D** and **E**). Consistent results were obtained with 786-O cells in which *PSAT1* was knocked out via CRISPR-Cas9 (Supplementary Figs. S12A–S12F and S13A–S13D). We observed a significant reduction in tumor growth when 786-O cells lacked *PSAT1*. In addition, *PSAT1* knockout cells exhibited smaller RCC tumors than those derived from wild-type ccRCC cells.

In summary, our findings support the role of serine biosynthesis in promoting tumor growth and metastasis. Sunitinib treatment triggers the activation of the GCN2–eIF2α–ATF4 signaling axis, which in turn stimulates the expression of serine synthesis enzymes, subsequently leading to increase *de novo* serine/glycine synthesis. This metabolic adaptation enables sunitinib-treated cells to withstand stress and persist by promoting nucleotide synthesis, a crucial pathway for sustaining anabolic metabolism and tumor cell survival. Furthermore, inhibition of PHGDH or reduction of PSAT1 levels not only led to decreased cell migration and invasion in metastatic ccRCC cell lines but also demonstrated efficacy in primary RCC cells. These findings reveal a mechanism through which kidney cancer cells persist under sunitinib therapy, involving a metabolic reprogramming that provides essential metabolite building blocks for tumor survival, resistance, and progression. Thus, this study could potentially inform future therapeutic strategies targeting serine and nucleotide synthesis pathways to enhance the efficacy of kidney cancer treatments.

Discussion

The intricate landscape of metabolic alterations in response to sunitinib has remained relatively elusive until now. Our study reveals how RCC cells metabolically adapt to sunitinib. Leveraging RNA-seq and metabolite profiling, we show that RCC cells, sensitive or resistant to sunitinib treatment, exhibit increased serine biosynthesis in sunitinib-treated RCC cells, which sustains tumor growth and progression. Indeed, numerous cancer cells, spanning various organs, heavily rely on serine and metabolite production. This unique dependency unveils promising therapeutic prospects,

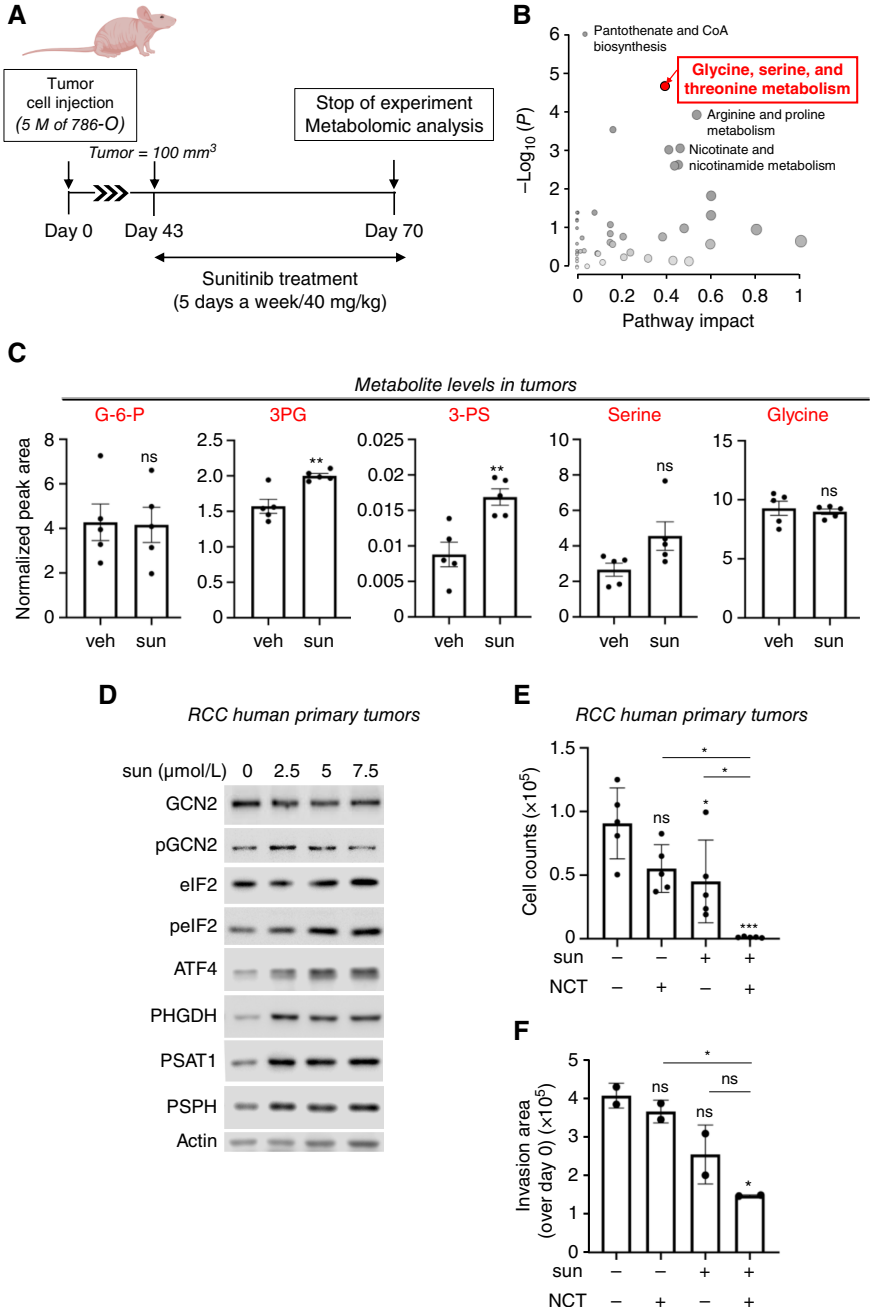

Figure 7.

Sunitinib enhances serine biosynthesis pathway *in vivo* and in ccRCC patient samples. **A,** Schematic of the *in vivo* experiment: 786-O cells were subcutaneously implanted into nude mice ($n = 5$ per group; two tumors per mouse). Mice were treated with either vehicle (veh) or sunitinib (40 mg/kg/day orally, 5 days a week, from day 42 to day 69). Metabolite profiling was conducted on tumor samples collected at the end of the treatment period. **B,** Bubble plots illustrating altered metabolic pathways in ccRCC xenografts. Pathway comparison between sunitinib-treated and control mice shows that glycine, serine, and threonine metabolism (highlighted in red) is one of the most impacted pathways. The size of each bubble corresponds to the pathway impact. **C,** Normalized peak areas of metabolites, including intermediates of the serine biosynthesis pathway in ccRCC xenograft models treated with vehicle (veh, DMSO) or sunitinib (sun). **D,** Immunoblots of fresh human kidney cells treated with DMSO (veh) or sunitinib at varying concentrations for 48 hours. The immunoblot is representative of four different fresh human kidney samples. **E,** Cell count performed 96 hours after treating fresh human kidney cells with DMSO (veh), sunitinib (5 μmol/L), or NCT-503 (NCT; 50 μmol/L), or a combination of both treatments. Five different experiments were conducted. **F,** Quantification of spheroid invasion areas after 7 days of invasion. Spheroids from ccRCC patient samples were treated with DMSO (veh), sunitinib (0.5 μmol/L), NCT-503 (30 μmol/L), or a combination of both treatments 24 hours before embedding in Matrigel (1 mg/mL). Two different experiments were conducted. ns, nonsignificant; *, $P < 0.05$; **, $P < 0.01$; ***, $P < 0.001$ (two-way ANOVA).

whether through inhibiting *de novo* serine synthesis or restricting the availability and uptake of exogenous serine.

Crucially, our study extends beyond RCC, revealing that sunitinib treatment enhances serine synthesis in diverse cancer models, including TNBC, lung cancer, medulloblastoma, and head and neck cancer. Mechanistically, sunitinib induces the ISR, activating the GCN2–ATF4 axis, thereby upregulating serine synthesis enzymes and stimulating serine synthesis.

Direct inhibition of serine biosynthesis emerges as a potent strategy, inhibiting tumor growth while curtailing cell migration and invasion. These findings not only deepen our understanding of the metabolic adaptations induced by sunitinib but also offer promising avenues for developing targeted therapies across a spectrum of aggressive cancers.

This study was performed on two RCC cell lines, 786-O and RCC10. 786-O, which was established as one of the first RCC cell lines, has many characteristics of ccRCC and is most commonly used in RCC research. Like the 786-O RCC line, the RCC10 line is also defective in VHL expression. We also performed an RNA-seq analysis in a third RCC line, A498, which also shows a defect in VHL expression. In our model, comprising three distinct cell lines resistant to sunitinib, we observed an elevation in the serine biosynthesis pathway. Interestingly, whereas

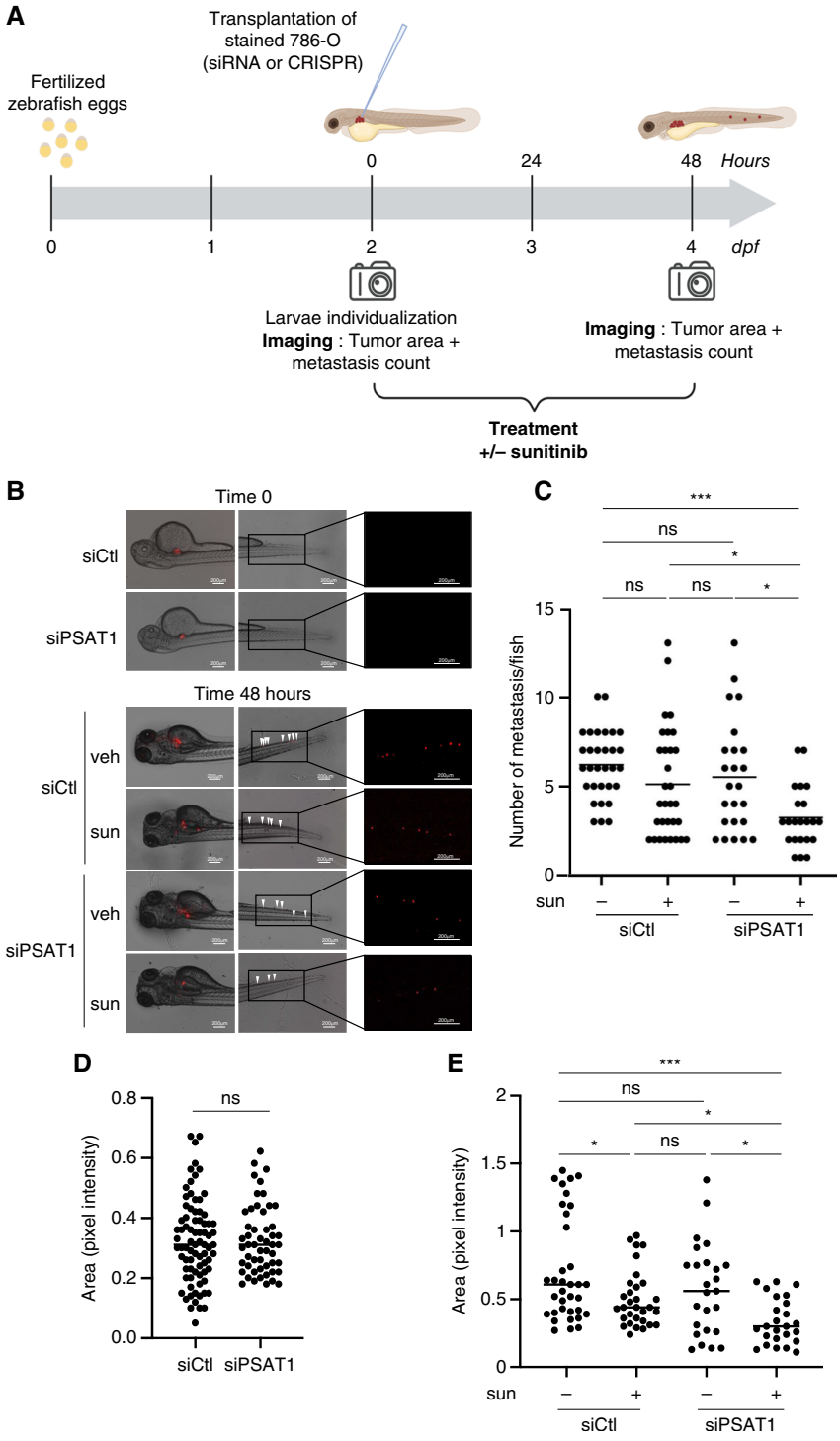

Figure 8.

PSAT1 depletion suppresses local growth and distant metastases in a zebrafish model. **A,** Schematic of the *in vivo* experiment: 786-O cells treated with siRNA (siPSAT1 or nontargeting siCtl) were injected into the perivitelline space of zebrafish embryos at 48-hpf. dpf, days post-fertilization. Embryos were treated with or without sunitinib (2.5 μmol/L), and tumor area and metastasis were assessed at 0 and 48 hours after injection. **B,** Representative images of local and distant metastases in zebrafish embryos ($N = 30$) injected with siCtl- or siPSAT1-treated 786-O cells (labeled with red DiD) into the perivitelline space and treated with sunitinib (2.5 μmol/L). Analysis was conducted at 0 and 48 hours later. **C,** Quantification of distant metastases per zebrafish, based on fluorescence microscopy. Five different experiments were conducted. **D** and **E,** Quantification of tumor growth by measuring tumor area and red fluorescent protein (RFP) signal area. ns, nonsignificant; *, $P < 0.05$; ***, $P < 0.001$ (two-way ANOVA). Five different experiments were conducted. **A,** Created in BioRender. Giuliano, S. (2025) https://BioRender.com/e83m090.

PSAT1 and *PSPH* exhibited an increase, *PHGDH* showed no significant change.

This led us to hypothesize that PHGDH might be regulated differently compared with PSAT1 and PSPH in our ccRCC model. Specifically, PHGDH regulation may be influenced by HIF2, whereas PSAT1 and PSPH could be modulated by the ISR pathway GCN2/eIF2/ATF4 in our ccRCC model (54–57). Notably, in contrast to our ccRCC model, other cancer cell lines demonstrated an increase in PSAT1, PSPH, and PHGDH with sunitinib treatment, suggesting that the regulation of PHGDH in response to sunitinib may be specific to RCC and unrelated to the treatment itself.

Although our findings shed light on these differential expressions, further studies are imperative to enhance our understanding of the intricate pathways governing the upregulation of the serine biosynthesis pathway in ccRCC.

ATF4 emerges as a pivotal transcriptional regulator of the serine synthesis pathway in various cancers (43, 44). In our model, we identified the GCN2 and eIF2 pathways as regulators of ATF4.

Although ATF4 presents a potential target for cancer treatment (58), direct ATF4 treatment is hindered by developmental defects observed in Atf4-null mice (59). Moreover, siRNA against *ATF4* resulted in rapid cell death in our model (Supplementary Fig. S14), suggesting that direct targeting of ATF4 may not be feasible.

In addition to the established functions of GCN2 and ATF4 in the sensing and control of amino acid metabolism, recent findings have shown that several TKIs, including sunitinib, can directly bind to and activate GCN2 (60). This activation triggers the phosphorylation of eIF2α, subsequently enhancing *ATF4* mRNA translation and upregulating the expression of genes involved in serine synthesis, such as *PSPH* and *PSAT1*. These observations provide a mechanistic basis for the GCN2–ATF4-dependent increased *de novo* serine synthesis upon sunitinib treatment. Therefore, targeting serine synthesis, in combination with sunitinib treatment, may be a therapeutic strategy to overcome resistance across various cancer types.

Mechanistically, sunitinib induces the ISR, activating the GCN2–ATF4 axis, which, in turn, upregulates serine synthesis enzymes and promotes serine synthesis. The direct inhibition of serine biosynthesis not only inhibits tumor growth but also limits cell migration and invasion. Importantly, our findings suggest that targeting the serine biosynthesis pathway could serve as a promising therapeutic strategy to overcome treatment resistance in RCC.

Recent evidence supports the use of immune checkpoint inhibitors in combination with targeted anti-VEGF agents for treating metastatic RCC. Axitinib, a TKI similar to sunitinib, did not induce upregulation of the serine biosynthesis pathway in RCC cells, in contrast to sunitinib (Supplementary Fig. S15). This discrepancy is attributed to the lysosomotropic properties of sunitinib, which is protonated at acidic pH, preventing its crossing of membranes. Lysosomal sequestration of sunitinib, a process not observed with axitinib, leads to incomplete autophagy, impacting the serine biosynthesis pathway (13). Recent studies by Ai-Ling Tian and colleagues (61) demonstrated that lysosomotropic agents, including azithromycin, chloroquine, and hydroxychloroquine, activate the ISR. Our initial findings suggest a process specific to lysosomotropic drugs, warranting further investigations to better comprehend the intricate relationship between lysosomotropic drugs and metabolic adaptations. Furthermore, our investigation into the impact of lysosomotropic drugs, specifically sunitinib, on the serine biosynthesis pathway reveals a unique relationship. Unlike other TKIs, sunitinib's lysosomal sequestration induces incomplete autophagy, affecting ATF4 expression and subsequently influencing serine biosynthesis. This intriguing link between lysosomotropic drugs and metabolic adaptations merits further exploration to better comprehend its implications in cancer treatment.

It is also important to note that intermediates of the serine synthesis pathway may be involved in the mechanisms underlying the resistance to sunitinib. For example, serine synthesis was shown to be essential for tricarboxylic acid (TCA) cycle function through the PSAT1-dependent production of α-ketoglutarate (αKG) under glutamine blockade (62). Whereas changes in serine synthesis rate can alter αKG levels and therefore TCA cycle activity, our metabolite profile did not show significant variations in αKG levels upon sunitinib treatment in sensitive and resistant cells. This suggests that the increase in serine synthesis upon sunitinib treatment does not contribute to αKG-dependent control of the TCA cycle, but further studies are warranted to definitively rule this possibility out (25).

In essence, our study sheds light on the dynamic interplay between sunitinib treatment, the serine biosynthesis pathway, and the ISR. These insights not only enhance our understanding of the metabolic mechanisms facilitating resistance to current therapies used against ccRCC but also unveil promising therapeutic strategies to counter resistance and tackle aggressive RCC by targeting the serine biosynthesis pathway.

In conclusion, our study demonstrates that sunitinib treatment of RCC and other cancer cell types, including TNBC, lung cancer, medulloblastoma, and head and neck cancer, leads to an increase in serine synthesis, enabling cell survival and continued growth. Therefore, cotargeting tyrosine kinase receptors and serine synthesis is a potential effective strategy to suppress more effectively the growth of tumors that are resistant to sunitinib.

Authors' Disclosures

No disclosures were reported.

Authors' Contributions

M. Teisseire: Formal analysis, investigation, methodology, writing–review and editing. **U. Sahu:** Formal analysis, investigation, methodology. **J. Parola:** Investigation. **M.-C. Tsai:** Resources, investigation. **V. Vial:** Investigation. **J. Durivault:** Resources, methodology. **R. Grépin:** Investigation. **Y. Cormerais:** Conceptualization, investigation. **C. Molina:** Investigation. **A. Gouraud:** Investigation. **G. Pagès:** Conceptualization, resources, supervision, funding acquisition, visualization, writing–original draft, writing–review and editing. **I. Ben-Sahra:** Conceptualization, resources, supervision, funding acquisition, investigation, visualization, methodology, writing–original draft, writing–review and editing. **S. Giuliano:** Conceptualization, resources, formal analysis, supervision, funding acquisition, validation, investigation, visualization, methodology, writing–original draft, writing–review and editing.

Acknowledgments

We extend our sincere thanks to the IRCAN core facilities, particularly the Animal Facility and the Cytometry Facility (CYTOMED), for their technical assistance. The CYTOMED facility has been supported by the Conseil Général 06, the FEDER, the Ministère de l'Enseignement Supérieur, the Région Provence-Alpes-Côte d'Azur, and INSERM. We also acknowledge MET'CONNECT, a Structuring Action financed by the French National Cancer Institute (INCa), the Région Sud, and the Canceropôle Provence-Alpes-Côte d'Azur. Metabolomics services were performed by the Metabolomics Core Facility at Robert H. Lurie Comprehensive Cancer Center of Northwestern University. This study was supported by the French Ministry of research and Fondation pour la Recherche Médicale, FRM (FDT202304016664 PhD grant MT). This work was supported by funding from the Fondation de France G. Pagès, the Fondation ARC "Equipe Labellisée" and the contract ARCAGEING2023020006332 (G. Pagès) and PJA20191209349 (S. Giuliano), the national agency of research France (ANR, JCJC contract, ANR-21-CE14-0008-01, S. Giuliano), the Ligue Nationale contre le Cancer Equipe labellisée 2019 G. Pagès, Canceropôle PACA (Emergence, 2019, S. Giuliano), UCA credits incitatifs (S. Giuliano), the NIH (R01GM135587 and R01GM143334-04; I. Ben-Sahra), and the American Cancer Society (DBG-23-1039959-01-TBE; I. Ben-Sahra). We support inclusive, diverse, and equitable conduct of research.

Note

Supplementary data for this article are available at Cancer Research Online (http://cancerres.aacrjournals.org/).

Received April 30, 2024; revised October 23, 2024; accepted February 21, 2025; posted first March 3, 2025.

References

1. Maxwell PH, Wiesener MS, Chang GW, Clifford SC, Vaux EC, Cockman ME, et al. The tumour suppressor protein VHL targets hypoxia-inducible factors for oxygen-dependent proteolysis. Nature 1999;399:271–5.
2. Kaelin WG Jr. Molecular basis of the VHL hereditary cancer syndrome. Nat Rev Cancer 2002;2:673–82.
3. Brugarolas J. PBRM1 and BAP1 as novel targets for renal cell carcinoma. Cancer J 2013;19:324–32.
4. Chowdhury B, Porter EG, Stewart JC, Ferreira CR, Schipma MJ, Dykhuizen EC. PBRM1 regulates the expression of genes involved in metabolism and cell adhesion in renal clear cell carcinoma. PLoS One 2016;11:e0153718.
5. Tang Y, Jin Y-H, Li H-L, Xin H, Chen J-D, Li X-Y, et al. PBRM1 deficiency oncogenic addiction is associated with activated AKT-mTOR signalling and aerobic glycolysis in clear cell renal cell carcinoma cells. J Cell Mol Med 2022; 26:3837–49.
6. Leisz S, Schulz K, Erb S, Oefner P, Dettmer K, Mougiakakos D, et al. Distinct von Hippel-Lindau gene and hypoxia-regulated alterations in gene and protein expression patterns of renal cell carcinoma and their effects on metabolism. Oncotarget 2015;6:11395–406.
7. Mullen NJ, Singh PK. Nucleotide metabolism: a pan-cancer metabolic dependency. Nat Rev Cancer 2023;23:275–94.
8. Pavlova NN, Zhu J, Thompson CB. The hallmarks of cancer metabolism: still emerging. Cell Metab 2022;34:355–77.
9. Escudier B, Porta C, Schmidinger M, Rioux-Leclercq N, Bex A, Khoo V, et al. Renal cell carcinoma: ESMO Clinical Practice Guidelines for diagnosis, treatment and follow-up. Ann Oncol 2019;30:706–20.
10. Kollmannsberger C, Soulieres D, Wong R, Scalera A, Gaspo R, Bjarnason G. Sunitinib therapy for metastatic renal cell carcinoma: recommendations for management of side effects. Can Urol Assoc J 2007;1(2 Suppl):S41–54.
11. Sehdev S. Sunitinib toxicity management – a practical approach. Can Urol Assoc J 2016;10:S248-51.
12. Motzer RJ, Hutson TE, Tomczak P, Michaelson MD, Bukowski RM, Oudard S, et al. Overall survival and updated results for sunitinib compared with interferon alfa in patients with metastatic renal cell carcinoma. J Clin Oncol 2009;27:3584–90.
13. Giuliano S, Cormerais Y, Dufies M, Grépin R, Colosetti P, Belaid A, et al. Resistance to sunitinib in renal clear cell carcinoma results from sequestration in lysosomes and inhibition of the autophagic flux. Autophagy 2015;11: 1891–904.
14. Wettersten HI, Aboud OA, Lara PN Jr, Weiss RH. Metabolic reprogramming in clear cell renal cell carcinoma. Nat Rev Nephrol 2017;13:410–9.
15. Reid MA, Allen AE, Liu S, Liberti MV, Liu P, Liu X, et al. Serine synthesis through PHGDH coordinates nucleotide levels by maintaining central carbon metabolism. Nat Commun 2018;9:5442.
16. Fan TWM, Bruntz RC, Yang Y, Song H, Chernyavskaya Y, Deng P, et al. De novo synthesis of serine and glycine fuels purine nucleotide biosynthesis in human lung cancer tissues. J Biol Chem 2019;294:13464–77.
17. DeBerardinis RJ. Serine metabolism: some tumors take the road less traveled. Cell Metab 2011;14:285–6.
18. Pan S, Fan M, Liu Z, Li X, Wang H. Serine, glycine and one-carbon metabolism in cancer (Review). Int J Oncol 2021;58:158–70.
19. Pacold ME, Brimacombe KR, Chan SH, Rohde JM, Lewis CA, Swier LJYM, et al. A PHGDH inhibitor reveals coordination of serine synthesis and one-carbon unit fate. Nat Chem Biol 2016;12:452–8.
20. Ou Y, Wang S-J, Jiang L, Zheng B, Gu W. p53 protein-mediated regulation of phosphoglycerate dehydrogenase (PHGDH) is crucial for the apoptotic response upon serine starvation. J Biol Chem 2015;290:457–66.
21. Frezza C. Cancer metabolism: addicted to serine. Nat Chem Biol 2016;12: 389–90.
22. Labuschagne CF, van den Broek NJF, Mackay GM, Vousden KH, Maddocks ODK. Serine, but not glycine, supports one-carbon metabolism and proliferation of cancer cells. Cell Rep 2014;7:1248–58.
23. Locasale JW, Grassian AR, Melman T, Lyssiotis CA, Mattaini KR, Bass AJ, et al. Phosphoglycerate dehydrogenase diverts glycolytic flux and contributes to oncogenesis. Nat Genet 2011;43:869–74.
24. Soflaee MH, Kesavan R, Sahu U, Tasdogan A, Villa E, Djabari Z, et al. Purine nucleotide depletion prompts cell migration by stimulating the serine synthesis pathway. Nat Commun 2022;13:2698.
25. Possemato R, Marks KM, Shaul YD, Pacold ME, Kim D, Birsoy K, et al. Functional genomics reveal that the serine synthesis pathway is essential in breast cancer. Nature 2011;476:346–50.
26. Mullarky E, Mattaini KR, Vander Heiden MG, Cantley LC, Locasale JW. PHGDH amplification and altered glucose metabolism in human melanoma. Pigment Cell Melanoma Res 2011;24:1112–5.
27. Rathore R, Schutt CR, Van Tine BA. PHGDH as a mechanism for resistance in metabolically-driven cancers. Cancer Drug Resist 2020;3:762–74.
28. Villa E, Sahu U, O'Hara BP, Ali ES, Helmin KA, Asara JM, et al. mTORC1 stimulates cell growth through SAM synthesis and m6A mRNA-dependent control of protein synthesis. Mol Cell 2021;81:2076–93.e9.
29. Weinberg SE, Singer BD, Steinert EM, Martinez CA, Mehta MM, Martínez-Reyes I, et al. Mitochondrial complex III is essential for suppressive function of regulatory T cells. Nature 2019;565:495–9.
30. Yuan M, Kremer DM, Huang H, Breitkopf SB, Ben-Sahra I, Manning BD, et al. Ex vivo and in vivo stable isotope labelling of central carbon metabolism and related pathways with analysis by LC-MS/MS. Nat Protoc 2019; 14:313–30.
31. Chong J, Wishart DS, Xia J. Using MetaboAnalyst 4.0 for comprehensive and integrative metabolomics data analysis. Curr Protoc Bioinformatics 2019;68:e86.
32. Labun K, Montague TG, Krause M, Torres Cleuren YN, Tjeldnes H, Valen E. CHOPCHOP v3: expanding the CRISPR web toolbox beyond genome editing. Nucleic Acids Res 2019;47:W171–W174.
33. Ran FA, Hsu PD, Wright J, Agarwala V, Scott DA, Zhang F. Genome engineering using the CRISPR-Cas9 system. Nat Protoc 2013;8:2281–308.
34. Grépin R, Ambrosetti D, Marsaud A, Gastaud L, Amiel J, Pedeutour F, et al. The relevance of testing the efficacy of anti-angiogenesis treatments on cells derived from primary tumors: a new method for the personalized treatment of renal cell carcinoma. PLoS One 2014;9:e89449.
35. Gotink KJ, Broxterman HJ, Labots M, de Haas RR, Dekker H, Honeywell RJ, et al. Lysosomal sequestration of sunitinib: a novel mechanism of drug resistance. Clin Cancer Res 2011;17:7337–46.
36. Amelio I, Cutruzzolá F, Antonov A, Agostini M, Melino G. Serine and glycine metabolism in cancer. Trends Biochem Sci 2014;39:191–8.
37. Locasale JW. Serine, glycine and one-carbon units: cancer metabolism in full circle. Nat Rev Cancer 2013;13:572–83.
38. Zhu H-L, Shi X-T, Xu X-F, Zhou G-X, Xiong Y-W, Yi S-J, et al. Melatonin protects against environmental stress-induced fetal growth restriction via suppressing ROS-mediated GCN2/ATF4/BNIP3-dependent mitophagy in placental trophoblasts. Redox Biol 2021;40:101854.
39. Masson GR. Towards a model of GCN2 activation. Biochem Soc Trans 2019; 47:1481–8.
40. Gao L, Chen J, Li J, Cui A-Q, Zhang W-W, Li X-L, et al. Microcystin-LR inhibits testosterone synthesis via reactive oxygen species-mediated GCN2/eIF2α pathway in mouse testes. Sci Total Environ 2021;781:146730.
41. Harding HP, Novoa I, Zhang Y, Zeng H, Wek R, Schapira M, et al. Regulated translation initiation controls stress-induced gene expression in mammalian cells. Mol Cell 2000;6:1099–108.
42. Harding HP, Zhang Y, Zeng H, Novoa I, Lu PD, Calfon M, et al. An integrated stress response regulates amino acid metabolism and resistance to oxidative stress. Mol Cell 2003;11:619–33.
43. DeNicola GM, Chen P-H, Mullarky E, Sudderth JA, Hu Z, Wu D, et al. NRF2 regulates serine biosynthesis in non-small cell lung cancer. Nat Genet 2015;47:1475–81.
44. Ye J, Mancuso A, Tong X, Ward PS, Fan J, Rabinowitz JD, et al. Pyruvate kinase M2 promotes de novo serine synthesis to sustain mTORC1 activity and cell proliferation. Proc Natl Acad Sci U S A 2012;109:6904–9.
45. Scheuner D, Song B, McEwen E, Liu C, Laybutt R, Gillespie P, et al. Translational control is required for the unfolded protein response and in vivo glucose homeostasis. Mol Cell 2001;7:1165–76.
46. Lu PD, Harding HP, Ron D. Translation reinitiation at alternative open reading frames regulates gene expression in an integrated stress response. J Cell Biol 2004;167:27–33.
47. Park Y, Reyna-Neyra A, Philippe L, Thoreen CC. mTORC1 balances cellular amino acid supply with demand for protein synthesis through post-transcriptional control of ATF4. Cell Rep 2017;19:1083–90.
48. Ben-Sahra I, Hoxhaj G, Ricoult SJH, Asara JM, Manning BD. mTORC1 induces purine synthesis through control of the mitochondrial tetrahydrofolate cycle. Science 2016;351:728–33.
49. Metcalf S, Dougherty S, Kruer T, Hasan N, Biyik-Sit R, Reynolds L, et al. Selective loss of phosphoserine aminotransferase 1 (PSAT1) suppresses

migration, invasion, and experimental metastasis in triple negative breast cancer. Clin Exp Metastasis 2020;37:187–97.
50. Zhu S, Wang X, Liu L, Ren G. Stabilization of Notch1 and β-catenin in response to ER- breast cancer-specific up-regulation of PSAT1 mediates distant metastasis. Transl Oncol 2022;20:101399.
51. Huang D, Ding Y, Li Y, Luo W-M, Zhang Z-F, Snider J, et al. Sunitinib acts primarily on tumor endothelium rather than tumor cells to inhibit the growth of renal cell carcinoma. Cancer Res 2010;70:1053–62.
52. Astell KR, Sieger D. Zebrafish in vivo models of cancer and metastasis. Cold Spring Harb Perspect Med 2020;10:a037077.
53. Astone M, Dankert EN, Alam SK, Hoeppner LH. Fishing for cures: the allure of using zebrafish to develop precision oncology therapies. NPJ Precis Oncol 2017;1:39.
54. Samanta D, Park Y, Andrabi SA, Shelton LM, Gilkes DM, Semenza GL. RETRACTED: PHGDH expression is required for mitochondrial redox homeostasis, breast cancer stem cell maintenance, and lung metastasis. Cancer Res 2016;76:4430–42.
55. Samanta D, Prabhakar NR, Semenza GL. Systems biology of oxygen homeostasis. Wiley Interdiscip Rev Syst Biol Med 2017;9:10.1002/wsbm.1382. https://doi.org/10.1002/wsbm.1382.
56. Semenza GL. Hypoxia-inducible factors: coupling glucose metabolism and redox regulation with induction of the breast cancer stem cell phenotype. EMBO J 2017;36:252–9.
57. Yoshino H, Nohata N, Miyamoto K, Yonemori M, Sakaguchi T, Sugita S, et al. PHGDH as a key enzyme for serine biosynthesis in HIF2α-targeting therapy for renal cell carcinoma. Cancer Res 2017;77:6321–9.
58. Yang M, Vousden KH. Serine and one-carbon metabolism in cancer. Nat Rev Cancer 2016;16:650–62.
59. Masuoka HC, Townes TM. Targeted disruption of the activating transcription factor 4 gene results in severe fetal anemia in mice. Blood 2002;99:736–45.
60. Tang CP, Clark O, Ferrarone JR, Campos C, Lalani AS, Chodera JD, et al. GCN2 kinase activation by ATP-competitive kinase inhibitors. Nat Chem Biol 2022;18:207–15.
61. Tian A-L, Wu Q, Liu P, Zhao L, Martins I, Kepp O, et al. Lysosomotropic agents including azithromycin, chloroquine and hydroxychloroquine activate the integrated stress response. Cell Death Dis 2021;12:6.
62. Qiu Y, Stamatatos OT, Hu Q, Ruiter Swain J, Russo S, Sann A, et al. The unique catalytic properties of PSAT1 mediate metabolic adaptation to glutamine blockade. Nat Metab 2024;6:1529–48.